



# Metamorphic origin of anastomosing and wavy laminae overprinting putative microbial deposits from the 3.22 Ga Moodies Group (Barberton Greenstone Belt)

Masafumi Saitoh<sup>a,b,c,\*</sup>, Nicolas Olivier<sup>a</sup>, Marion Garçon<sup>a</sup>, Maud Boyet<sup>a</sup>, Christophe Thomazo<sup>d,e</sup>, Julien Alleon<sup>b</sup>, Jean-François Moyen<sup>f</sup>, Vincent Motto-Ros<sup>g</sup>, Johanna Marin-Carbonne<sup>b</sup>

<sup>a</sup> Université Clermont Auvergne, CNRS, IRD, Laboratoire Magmas et Volcans, F-63000 Clermont-Ferrand, France

<sup>b</sup> Institut des Sciences de la Terre, Faculté des géosciences et de l'environnement, Université de Lausanne, 1015 Lausanne, Switzerland

<sup>c</sup> Earth-Life Science Institute, Tokyo Institute of Technology, 152-8550 Tokyo, Japan

<sup>d</sup> Laboratoire Biogéosciences, Université Bourgogne Franche-Comté, Dijon, France

<sup>e</sup> Institut Universitaire de France, 1 rue Descartes, 75231 Paris CEDEX 05, France

<sup>f</sup> Université de Lyon, UJM, UCBL, ENSL, CNRS, LGL-TPE, 23 rue Dr. Paul Michelon, F-42023, Saint-Étienne, France

<sup>g</sup> Université Lyon, Université Claude Bernard Lyon 1, CNRS, Institut Lumière Matière, UMR 5306, F-69622 Villeurbanne, France

## ARTICLE INFO

### Keywords:

Paleoarchean  
Barberton Greenstone Belt  
Moodies Group  
Anastomosing and wavy laminae  
Metasomatism

## ABSTRACT

Anastomosing branching and wavy laminae in quartz-rich sandstones of the 3.22 Ga Moodies Group in the Barberton Greenstone Belt (BGB), South Africa, have been extensively described as fossilized microbial mats developed in terrestrial to marine transitional environments. Petrological and geochemical characteristics of a ~ 350 m thick Moodies succession in the Saddleback Syncline in the central BGB were analyzed to reconstruct the post-depositional history of the sediments and to better constrain the origin of the laminae. The studied sandstones are composed mainly of quartz, potassium feldspar, and chert clastic grains with various proportions of microquartz and sericite cements. In coastal floodplain and inter- to supra-tidal environments, quiescent periods with low current velocity allowed the repeated deposition of thin (<5 mm thick) and fine-grained laminae with clay matrix and potentially organic matter. In contrast, subtidal settings under consistently high-energy conditions led to the deposition of coarse- to medium-sized sands without fine-grained laminae. Intergrain areas in those coarse sediments were infilled with a microquartz cement during burial diagenesis. Due to the presence of clay matrix, the fine-grained laminae had a reduced porosity that prevented the microquartz cementation within the laminae. This original clay matrix was later replaced with sericite cements during metamorphism, forming the anastomosing and wavy laminae observed at the hand-specimen scale in the studied sandstones. Microscopic dark areas within the laminae are composed mostly of opaque minerals with scarce carbonaceous material. The scarcity of carbonaceous material and the fluctuating energy settings, potentially inauspicious for the continuous development and preservation of biomats, are not in favor of a flourishing Paleoarchean microbial life on the Moodies sediments.

## 1. Introduction

Among the various clues to understand the record of traces of life on early Earth, ancient microbial biofilms and microbially induced sedimentary structures (MISS) have been a subject in numerous studies over the last 15 years (e.g., Noffke et al., 2003, 2008; Noffke, 2007; Wacey, 2009; Hickman-Lewis et al., 2018; Lepot, 2020). The development of

these structures depends largely on the depositional setting through colonization of biofilms and their potential physical interactions with clastic grains (Noffke et al., 2001). Some Archean rocks are composed of siliciclastic sediments deposited in tidal and shallow shelf settings that may have been favorable to the development of biofilms (e.g., Noffke, 2007, 2010; Noffke et al., 2013; Westall, 2008; Westall et al., 2011). However, the preservation of Archean biofilms and/or MISS required

\* Corresponding author at: Present address: School of Geosciences and Civil Engineering, Kanazawa University, Kakuma, Kanazawa 920-1192, Japan.  
E-mail address: [msaitoh@se.kanazawa-u.ac.jp](mailto:msaitoh@se.kanazawa-u.ac.jp) (M. Saitoh).

<https://doi.org/10.1016/j.precamres.2021.106306>

Received 15 December 2020; Received in revised form 8 June 2021; Accepted 8 June 2021

Available online 8 July 2021

0301-9268/© 2021 The Author(s).

Published by Elsevier B.V. This is an open access article under the CC BY-NC-ND license

(<http://creativecommons.org/licenses/by-nc-nd/4.0/>).

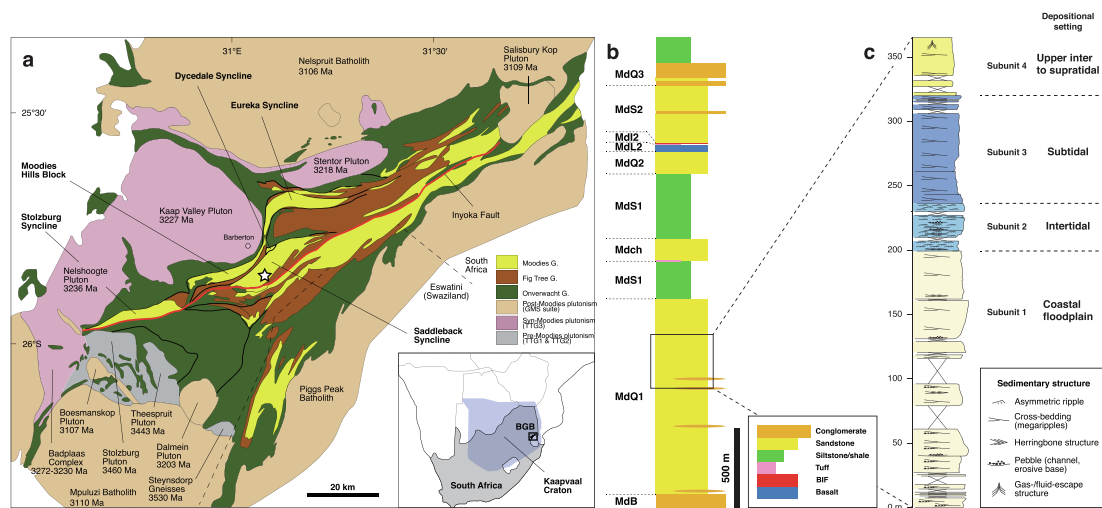


**Fig. 1.** Geological map (a) and stratigraphy (b, c) of the Moodies Group. (a) Simplified geological map of the Barberton Greenstone Belt (BGB) in northeast South Africa. The map is an enlarged square in the inset. A star shows the sampling locality in this study. (b) General stratigraphy of the Moodies Group in the Saddleback Syncline. (c) The analyzed sandstones in this study with sedimentary environments (according to Homman et al., 2015). Figures (a) and (b) are modified from Homann et al. (2015).

specific and complex taphonomic processes and their biogenicity has often been debated (e.g., Bower, 2011; Mariotti et al., 2014; Davies et al., 2016, 2018; Noffke, 2018; Westall et al., 2018; Hickman-Lewis et al., 2019).

Noffke et al. (2006) first proposed that wrinkle and roll-up sedimentary structures in the ~3.22 Ga Moodies Group in the Barberton Greenstone Belt (BGB), South Africa, were MISS. Heubeck (2009) subsequently interpreted that ubiquitous green anastomosing branching and wavy laminae in the Moodies sandstones were remnants of microbial mats. Homann et al. (2015) classified the laminae into three morphotypes and suggested a relationship between the mat morphologies and their associated depositional environments. A systematic difference in carbon and nitrogen isotopic composition between the terrestrial and marine deposits was also observed and interpreted to reflect the oldest evidence for the co-existence of distinctive terrestrial and marine ecosystems (Homann et al., 2018; Homann, 2019; Thomazo et al., 2020).

The BGB has undergone lower greenschist-facies regional metamorphism (<350 °C) and has a complex thermal history (e.g., de Ronde and de Wit, 1994), such as the emplacement of several plutonic domains

around the BGB at 3.23–3.21 Ga (Fig. 1a) (e.g., de Ronde and de Wit, 1994; Cutts et al., 2014; Moyen et al., 2019), followed by multiple tectono-thermal events during the Mesoarchean to Paleoproterozoic (Weis and Wasserburg, 1987; de Ronde et al., 1991a; Lécuyer et al., 1994; Toulkeridis et al., 1994, 1998). The Moodies sediments in the BGB were presumably affected by complex post-depositional processes, including polymetamorphism and more recent alteration via fluid circulations (e.g., Heubeck, 2019; Bonnand et al., 2020); however, the influence of post-depositional processes on the Moodies rocks has not yet been examined in detail.

In this study, we analyzed the microfacies and major and trace element composition of the lamina-bearing Moodies sandstones. Based on petrological and geochemical results, we reconstructed multiple post-depositional processes of the analyzed sandstones in association with their depositional settings and with the regional metamorphic history of the BGB. They enabled us to discuss the origin of the anastomosing and wavy laminae in the Moodies rocks in the framework of their post-depositional history.

## 2. Geological setting

The BGB at the Makhonjwa Mountains is located in northeastern South Africa and northern Eswatini (Swaziland) near the eastern margin of the Kaapvaal Craton (Fig. 1a). It is one of the best-preserved Paleoproterozoic greenstone belts consisting of a >10 km thick succession of interlayered volcanic and sedimentary rocks, termed the Barberton Supergroup (e.g., Lowe et al., 1999; Hofmann, 2005). The Barberton Supergroup (ca. 3.55 to 3.22 Ga) is subdivided (in ascending order) into the Onverwacht, the Fig Tree, and the Moodies groups. The Onverwacht Group (ca. 3.55 to 3.26 Ga) is composed mainly of mafic to ultramafic volcanic rocks (basalts and komatiites) with interlayered cherts and rare felsic volcanics as well as very few clastic units. The lithologically diverse Fig Tree Group (ca. 3.26 to 3.23 Ga) includes clastic sedimentary rocks (shales, sandstones and conglomerates), immature volcanoclastics, intermediate to felsic lavas, banded iron formations, barite, and cherts. The Moodies Group (ca. 3.22 Ga) is ~3.7 km thick and consists mainly of quartz-rich sandstones and siltstones with subordinate conglomerates, felsic volcanics, shales and jaspilites (Fig. 1b) (e.g., Eriksson, 1977, 1979, 1980; Heubeck and Lowe, 1994a, 1994b, 1999; Homann et al., 2015; Heubeck, 2019). The BGB is tightly folded; the central belt consists of a series of synclines, mostly cored by Moodies Group strata and separated by strike faults replacing tight anticlines (Anhaeusser et al.,

**Table 1**  
Stratigraphic units of the Moodies Group in the Eureka Syncline (Anhaeusser, 1976).

	Typical rock type	General lithological description
MdQ4	sandstone	sandstones, grits, small-pebble conglomerates
MdS3	shale	subgreywackes, coarse and fine sandstones shales, magnetic shales, phyllites, grits
MdQ3	quartzite	conglomerates, grits, quartzites, shaly partings
MdS2	shale	shales, phyllites, subgreywackes, dark shaly quartzites
MdI2	jaspilitic iron-formation	banded magnetic jaspilites, banded iron-formation, ferruginous and magnetic shales
MdL2	basaltic lava	massive and amygdaloidal lava
MdQ2	quartzite	conglomerates, gravel, grits, sandstones, quartzites
MdI1	jaspilitic iron-formation	banded magnetic jaspilites, banded iron-formation, ferruginous and magnetic shales
MdS1	shale	subgreywackes, sandy shales, finely laminated shales, dark shaly quartzites
MdQ1	felspathic quartzite	conglomerates, grits, felspathic quartzites, sandstones
MdCq	calcareous quartzite	carbonate-rich quartzites, marble, quartzo-felspathic sandstones
MdB	basal conglomerate	conglomerates, quartzites, subgreywackes

1981; Heubeck and Lowe, 1994a).

The Moodies Group has been suggested to be the oldest terrestrial to marine transitional sedimentary succession (e.g., Eriksson, 1977, 1979, 1980; Heubeck and Lowe, 1994a; Eriksson and Simpson, 2000; Eriksson et al., 2006; Simpson et al., 2012; Homann et al., 2015; Heubeck, 2019). Heubeck et al. (2013) indicated that the entire Moodies Group accumulated very rapidly (within <1–14 million years) at ~3.22 Ga, based on the dating of zircons in intercalated tuff beds of the sedimentary succession. North of the Inyoka Fault, a major divide in the BGB, the Moodies Group is exposed in several tectonic units, including (from northeast to southwest) the Eureka Syncline, Dycedale Syncline, Saddleback Syncline, Moodies Hills Block, and Stolzberg Syncline (e.g., Homann et al., 2015; Heubeck et al., 2016).

In the present study, we focused on a Moodies sedimentary succession in the Saddleback Syncline in the central BGB (Fig. 1). The ~3000 m thick Moodies Group is exposed continuously along the NE-SW trending syncline (Homann et al., 2015; Heubeck, 2019). In the Saddleback Syncline, the bottom 50–80 m thick part of the Moodies Group is composed mainly of interbedded cobble conglomerates and sandstones (Fig. 1b). These basal conglomerates are correlated to the MdB unit of the group in the northern Eureka Syncline (Table 1) (Anhaeusser, 1976; Homann et al., 2015), and are thought to have been deposited in a fluvial to alluvial setting (Eriksson, 1980; Heubeck and Lowe, 1994a). This conglomerate unit is overlain by ~1000 m thick quartz-rich sandstones in the lower part of the Saddleback succession. These sandstones are correlated to the MdQ1 unit of the Eureka succession (Anhaeusser, 1976; Homann et al., 2015), and would have been deposited on coastal floodplain to subtidal settings (Homann et al., 2015). Anastomosing branching and wavy laminae are frequently observed in these sandstones and are interpreted to be remnants of original microbial mats (Noffke et al., 2006; Heubeck, 2009; Homann et al., 2015).

The overlying 400–1000 m thick interval is composed mainly of fine-grained sandstones and siltstones and is correlated to the MdS1 unit of the Moodies Group (Fig. 1b) (Anhaeusser, 1976). This interval was deposited on a prodelta slope below the wave base (Heubeck, 2019). The MdS1 sandstones and siltstones are overlain by up to 150 m thick quartzarenites, which is correlated to the MdQ2 unit in the Eureka Syncline (Anhaeusser, 1976). The MdQ2 unit is interpreted as reflecting subtidal and intertidal settings (Eriksson, 1977), or an offshore subaqueous dune field (Heubeck and Lowe, 1994a). The MdQ2 arenites are overlain by a basaltic lava (MdL2 in Anhaeusser, 1976). This characteristic MdL2 lava is then overlain by banded iron formation (BIF), jaspilite, shale and siltstone (MdI2 in Anhaeusser, 1976). The MdI2 unit is overlain by ~300 m thick sandstones with conglomerates and siltstones, and these conglomerates and siltstones are correlated to the MdS2 unit (Anhaeusser, 1976). The uppermost Moodies succession in the Saddleback Syncline is characterized by up to 100 m thick quartzarenites and conglomerates (MdQ3).

### 3. Analyzed sedimentary succession and its depositional settings

In the present study, we analyzed a ~350 m thick succession in the upper part of the MdQ1 unit of the lower Moodies Group (25°50'19.9" S, 31°05'01.1" E) (Figs. 1c and 2a) (Anhaeusser, 1976; Homann et al., 2015). The MdQ1 unit is ~1000 m thick and is composed mostly of quartz-rich sandstones. This MdQ1 unit corresponds to the MD1 unit of alluvial plain facies in Eriksson (1978). Heubeck et al. (2013) interpreted that the MdQ1 sediments were deposited in a braided fluvial system. Heubeck (2009) subdivided the MdQ1 unit into four subunits based on the lithofacies and reconstructed their depositional settings: a coastal floodplain (subunit 1), a tidal coast (subunit 2), and subtidal and shoreface settings (subunits 3 and 4) (Table S1). Gamper et al. (2011) substantially changed the interpretation of their depositional settings: a terrestrial coastal zone (subunit 1), a subtidal to intertidal zone (subunit 2), and a nearshore zone (subunits 3 and 4). Homann et al. (2015) later

revised these depositional settings based on macroscopic lithofacies description: a coastal floodplain (subunit 1), an intertidal zone (subunit 2), a subtidal zone (subunits 3), and an upper inter- to supra-tidal zone (subunit 4) (Fig. 1c). The analyzed succession in the present study includes the four subunits of the MdQ1 unit and corresponds to stratigraphic Log 9 in Homann et al. (2015) in the central Saddleback Syncline. In this study, we follow the interpretation of depositional setting of the analyzed four subunits in Homann et al. (2015) (Figs. 1c and 2a).

The lowermost subunit 1 is ~200 m thick and is composed of coarse- to fine-grained sandstones. Cross-bedding, herringbone structures, and channels with erosive base are observed on the outcrop. Pebbles are most commonly observed in the lower part of the subunit (Fig. 2b). Anastomosing branching and wavy laminations are frequently recognized at the hand-specimen scale (Fig. 2c). Homann et al. (2015) interpreted the environment of the subunit 1 as a coastal floodplain, based notably on low-angle planar and trough cross-bedding and lenticular conglomerates with desiccation cracks.

The overlying subunit 2 is ~40 m thick and consists of medium-grained sandstones (Figs. 1c and 2d). Abundant asymmetric ripples, common herringbone structures, and some small and local pebbles are observed. Green anastomosing branching and wavy laminations at the hand-specimen scale are recognized. Based on the presence of herringbone cross-bedding, sigmoidal foresets, and mud drapes, Homann et al. (2015) suggested that the subunit 2 accumulated in an intertidal setting.

The ~80 m thick subunit 3 is composed mainly of medium- to fine-grained sandstones (Fig. 1c). Large cross-beddings are frequently observed through the subunit (Fig. 2e). As observed in Homann et al. (2015), this subunit is characterized by the lack of anastomosing branching and wavy laminations. The authors constrained its depositional environment to a subtidal setting, based on large-scale and low-angle planar foresets and putative gutter casts.

The uppermost subunit 4 is ~40 m thick and consists of medium-grained sandstones (Fig. 1c). Cross-beddings and subvertical gas/fluid-escape structures are frequently observed (Figs. 2f and g). Some anastomosing branching and wavy laminae are recognized. This subunit 4 corresponds to the basal part of the MD3 unit in Eriksson (1979), in which this part was interpreted to be a delta-front sediment. Homann et al. (2015) reinterpreted the depositional setting of the subunit 4 as an upper inter- to supra-tidal setting, based on abundant desiccation cracks in the subunit. A slight difference in thickness of the subunits 2 and 3 is observed between Log 9 in Homann et al. (2015) and the present log (Fig. 1c). This could be explained by substantial lateral changes in thicknesses of sedimentary bodies (megaripples and dunes) that form these subunits.

### 4. Materials and analytical methods

Forty-two rock samples were collected from the analyzed Saddleback succession. A part of these samples has been previously analyzed for quadruple sulfur isotope geochemistry (Saitoh et al., 2020). The lithofacies of all the collected rocks was observed in detail via optical microscopy. The proportion of grain to matrix/cement in the rocks was estimated according to Baccelle and Bosellini (1965). In addition to the microfacies description, multiple geochemical analyses (Raman spectroscopy, EPMA, SEM-EDS, LIBS, ICP-OES, ICP-MS, and EA) were conducted on a selected subset of the collected rock series.

#### 4.1. Raman spectroscopy

Eight samples in the analyzed succession (SAD4, 6, 20, 21, 26, 34, 39, and 40) were analyzed by Raman spectroscopy at the Laboratoire Magmas et Volcans (LMV), Clermont-Ferrand, France. Raman spectra were collected using a Renishaw InVia confocal Raman microspectrometer equipped with a 532 nm laser source, a Peltier-cooled CCD detector, an edge filter, a motorized XYZ stage and a Leica DM



Fig. 2. Outcrop photos of the analyzed Moodies sandstones. (a) A distant outcrop view of the sampling locality in the central Saddleback Syncline (the same hill of the stratigraphic Log 9 in Homann et al., 2015). The Moodies strata are dip subvertically and overturned. A person (circled) for scale. (b) Conglomerate (lower part) and megaripple (upper part) in the subunit 1. (c) Anastomosing and wavy laminae in the subunit 1. (d) Small channel, small megaripples, and flat laminae with ripples in the subunit 2. (e) Large-scale cross-bedding in the subunit 3. (f, g) gas-/fluid-escape structures in the subunit 4. A hammer (f) and pen (g) for scale are 28-cm- and 12-cm-long, respectively.

2500 M optical microscope. Scattered light was collected by a back-scattered geometry. Laser power on the sample was reduced by filters in order to operate at powers  $<1$  mW. We used a 1200 grooves/mm grating, which results in a spectral resolution better than  $1\text{ cm}^{-1}$ . The slit

aperture was set either to  $20\text{ }\mu\text{m}$  (high confocality setting) or  $65\text{ }\mu\text{m}$  (standard confocality setting) depending on grain size. A  $100\times$  microscope objective was used. These analytical conditions result in lateral and vertical spatial resolutions of  $<1\text{ }\mu\text{m}$  and  $2\text{ }\mu\text{m}$ , respectively. Daily

calibration of the spectrometer was performed based on a Si 520.7  $\text{cm}^{-1}$  peak. All spectra were recorded in the 95–2695  $\text{cm}^{-1}$  wavenumber range and from  $\sim 1050$  to 3400  $\text{cm}^{-1}$  in presence of carbonaceous matter, using WIRE<sup>TM</sup> 4.4 software. The number of acquisitions on a single spot varied from three to fifteen, and the duration of each acquisition ranged between 5 s and 30 s. Ninety-eight spots were measured in total in the selected eight samples. 2D maps were acquired on several areas using a 0.8  $\mu\text{m}$  or a 2  $\mu\text{m}$  step between points. Mineral identification was performed by comparison with standard spectra from the WIRE and RRUFF databases.

#### 4.2. Electron probe micro analyzer (EPMA)

Selected nine samples were analyzed by EPMA at the University of Lausanne, Switzerland. Quantitative spot analyses for Si, Mg, Na, K, Al, Ti, Fe, Ca, and Cr were conducted for five samples (SAD5, 22, 32, 37, and 39) with a JEOL 8230F microprobe, using a beam current of 400nA and an accelerating voltage of 15 kV, with a dwell time of 100 ms. Lab standard minerals (albite for Si and Na, forsterite for Mg, orthoclase for K and Al, TiO<sub>2</sub> for Ti, fayalite for Fe, anorthite for Ca, and chromite for Cr) were used for spot analyses. Moreover, X-ray compositional maps for Si, Mg, Na, K, Al, Ti, and Fe were obtained for five samples (SAD20, 23, 26, 34, and 39) with the same analytical conditions.

#### 4.3. Scanning electron microscopy (SEM) and energy dispersive spectroscopy (EDS)

SEM-EDS measurements were conducted for five samples in the subunits 1 and 2 at the University of Lausanne, using a Tescan Mira LMU SEM equipped with the Oxford Instruments AZtec 3.4 software package, to identify mineral phases in the sandstones. The measurements were operated at 20 kV acceleration voltage,  $\sim 6$  pA probe current, and 21 mm working distance. Backscattered electron (BSE) images were taken on finely polished thin sections coated with a 15 nm carbon layer, and the EDS analyses were carried out on them to determine the chemical composition of minerals in the analyzed areas. We conducted both spot analyses and semi quantitative elemental mapping, and the spatial distribution of Si, K, Al, Na, Ti, Fe, and Mg were visualized in the maps.

#### 4.4. Laser-induced breakdown spectroscopy (LIBS) imaging

LIBS imaging analyses were conducted for one sample from the subunit 2 at the Institute of Light and Matter, Lyon, France. In LIBS imaging, a series of laser-induced plasma is generated at different positions on the sample. Such plasma sources allow specific optical responses resulting from the electronic relaxation of atoms and ions excited by the high plasma temperature to be elicited from the elements constituting the sample. The light emitted by the plasma is collected and analyzed using an optical spectrometer equipped with an intensified charge-coupled device (ICCD) camera. The elemental “signal” (atomic and ionic emissions) is then extracted from the recorded spectra, and elemental maps can be obtained in a pixel-by-pixel manner (Sancey et al., 2014; Fabre et al., 2018; Motto-Ros et al., 2020). The sandstone sample was analyzed using Nd:YAG laser with pulse energy of about 600  $\mu\text{J}$  operating at 100 Hz, and a lateral resolution (i.e. distance between two consecutive laser shots) of 25  $\mu\text{m}$ . Two different Czerny-Turner spectrometers were used in order to detect intense lines of Al (309.2 nm), B (208.9 nm), Cr (267.7 nm), Fe (302.0 nm) and Ti (323.4 nm), among others.

#### 4.5. Major and trace element geochemistry

Fresh parts of the rock samples were carefully selected for major and trace element measurements and cut to remove weathered surfaces. The rock pieces were crushed into small chips (<1 cm in diameter) and were ultrasonically cleaned with distilled water and subsequently with pure

acetone. The cleaned chips were then powdered using an agate mill. Up to 25 g of powder was prepared for each sample. Twenty-nine samples from the four subunits were selected for major element analyses at the LMV in Clermont-Ferrand. Sample powder (100 mg) was mixed with LiBO<sub>2</sub> flux (300 mg) and fused at 1100 °C. The solutions were analyzed using the LMV HORIBA-Jobin-Yvon ULTIMA-C Inductively Coupled Plasma Optical Emission Spectrometer (ICP-OES). The precision and accuracy were determined from repeated measurements of the BHVO-1 reference material. Results are consistent within 3% of the certified data except for K<sub>2</sub>O (4%). The total volatile content (loss on ignition) was determined from 1 g of sample powder.

Trace elements were measured on twelve samples from the four subunits at the LMV. About 50 mg of sample powder were digested using ammonium bifluoride (Zhang et al., 2012). Closed savillex Teflon vials were placed into an oven at 220 °C for 24 h. After cooling, samples were dissolved in concentrated HNO<sub>3</sub> and evaporated to dryness several times. All measurements were performed using the LMV Agilent Inductively Coupled Plasma Mass Spectrometer (ICP-MS) in Clermont-Ferrand, France. Samples and certified rock standard were measured in 0.5 M-HNO<sub>3</sub>–0.05 M-HF with a dilution factor of about 3,500. Counts per second were calibrated using certified rock standards BHVO-2. The blank and reference materials (BE-N, BIR-1 and BHVO-2) were measured every three samples. Measurements were corrected from oxide interferences and instrumental drift if significant. The precision and accuracy were determined from four repeated measurements of the BE-N and BIR-1. Results are consistent within 4% of published data, except for U, Th, and Pb (<10%).

Trace element concentrations of the analyzed sandstones were normalized to upper continental crust (UCC) composition (Rudnick and Gao, 2014), and their rare-earth element (REE) concentrations were normalized to Chondrite and to Mud from Queensland (MuQ) (McDonough and Sun, 1995; Kamber et al., 2005).

#### 4.6. Elemental analyzer (EA)

For three samples from the subunits 1, 3, and 4, total organic carbon (TOC) contents were analyzed by EA. Powdered samples ( $\sim 0.5$  g) were reacted with 6 N HCl at room temperature for >12 h to remove carbonate at the LMV. The residue was cleaned by repeated centrifugation with ultrapure water and was then reacted with 46 M HF at 55 °C for >48 h to dissolve silicate. The residue was cleaned by repeated centrifugation with ultrapure water and was dried at 55 °C for >12 h. Aliquots of the dried residue (1–20 mg) were weighed in a tin capsule and their TOC contents were measured by a vario MICRO cube elemental analyzer (Elementar GmbH, Hanau, Germany) at Laboratoire Biogéosciences, Université Bourgogne Franche-Comté, Dijon, France. USGS40-certified reference material (C = 40.8 wt%) was used for calibration and the TOC content is shown as a dry weight percentage of the total fraction. The analytical reproducibility, based on duplicate analyses of USGS40, is better than 0.1 wt% (1 $\sigma$ ) for the residue.

## 5. Results

### 5.1. Petrological description

#### 5.1.1. Clastic grains

The analyzed Moodies succession is composed mostly of sandstones with some conglomerates (Figs. 1–3). The sandstones contain abundant coarse to very fine sand-size clastic grains. The grains range in size mostly from 100 to 1000  $\mu\text{m}$ . Those clastic grains are mainly quartz (>50%) (Figs. 3a and 3b). Potassium (K) feldspar (microcline and orthoclase) (<25%) and chert grains (<15%) are also frequently observed and the latter consist mostly of microquartz crystals with intracrystalline fine sericite (Figs. 3c and d). As some chert grains include substantial amounts (>5%) of sericite, Heubeck and Lowe (1999) described them originally as “quartz-sericite (QS) grains”. A

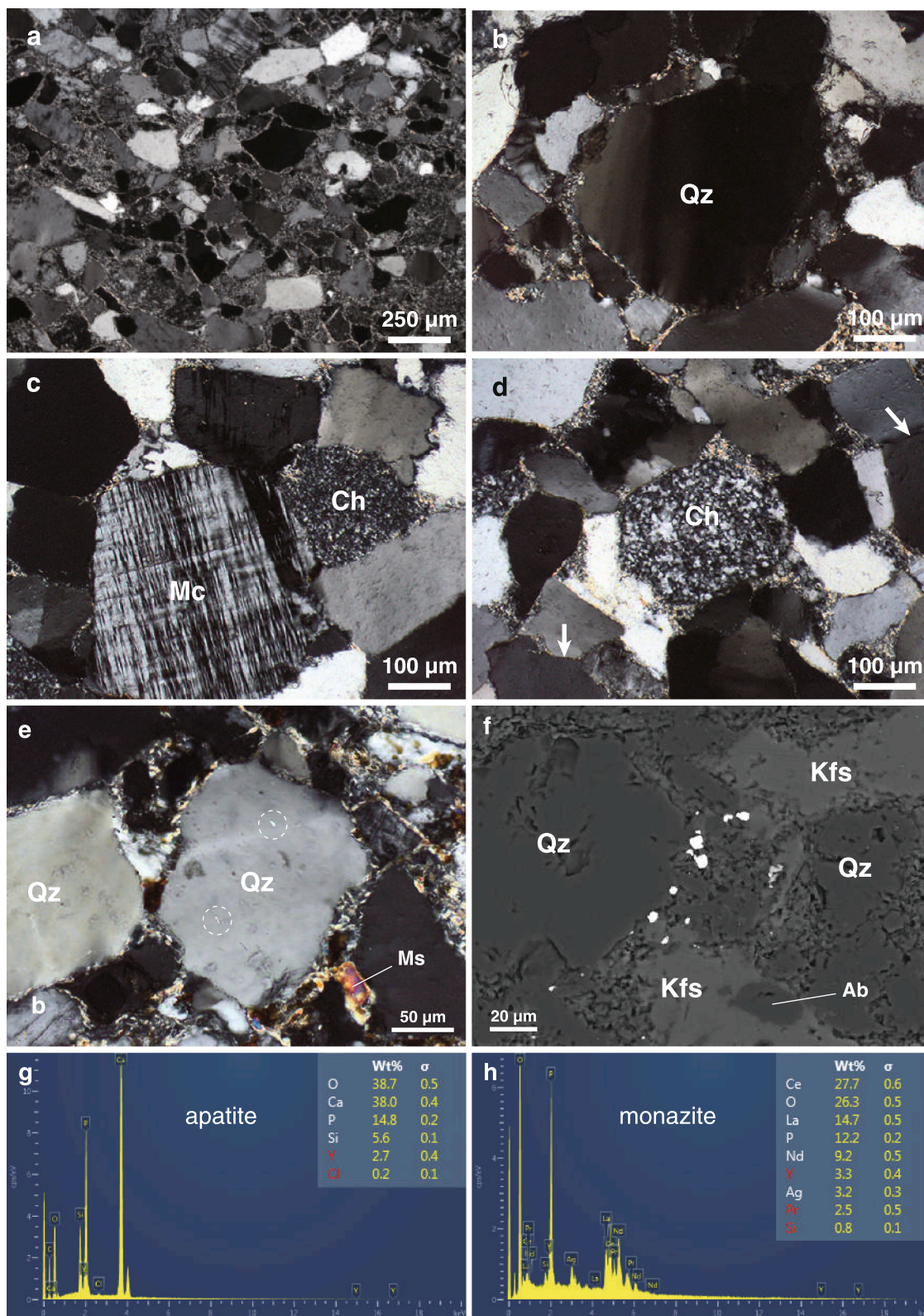


**Fig. 3.** Clastic grains of the analyzed sandstones. (a) Typical medium-grained quartz-rich sandstones (crossed nicols). (b) A quartz (Qz) grain with wavy extinction (crossed nicols). (c) A microcline (Mc) grain (crossed nicols). A chert (Ch) grain is also surrounded by quartz grains in the right side. (d) A rounded chert grain (crossed nicols). Arrows show intergranular pressure solution (IPS) texture. (e) Apatite inclusions (circled) in a quartz grain. Muscovite (Ms) is also shown. (f) BSE image of monazite-Ce (white grains). A partly albitized (Ab) K-feldspar (Kfs) is also shown. (g, h) EDS spectra of an apatite inclusion in quartz (g) and of monazite-Ce (h).

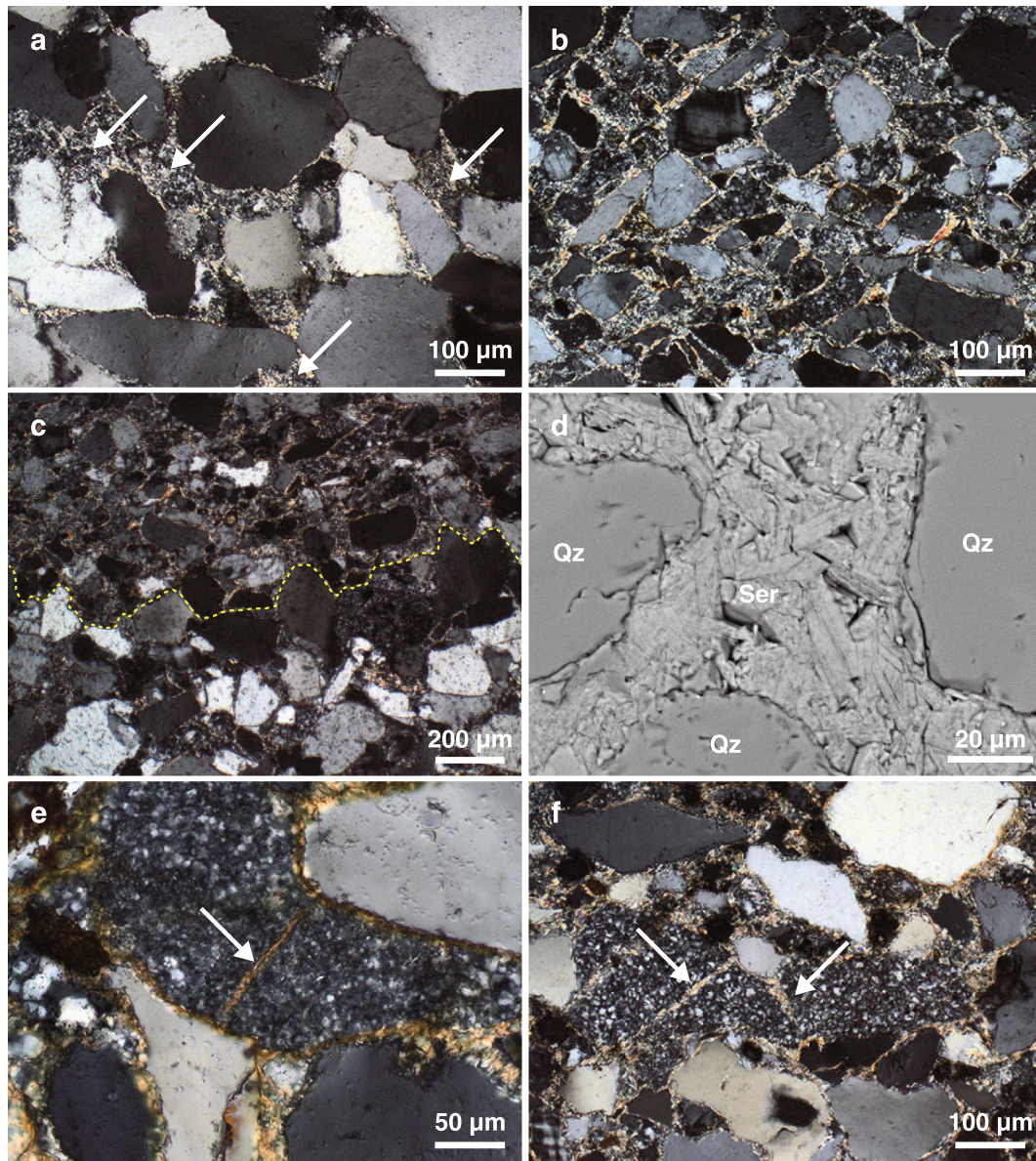


**Fig. 4.** Cements in the analyzed sandstones (crossed nicols except for d). (a) Coarse-grained sandstone with microquartz cements (arrows) in the subunit 3. (b) Fine-grained lamina enriched in sericite. (c) Boundary between lower coarse sediments and an upper fine-grained lamina enriched in sericite (intergranular brown crystal). (d) BSE image of elongated sericite (Ser) crystals between quartz (Qz) grains. (e, f) Sericite-bearing veins cutting irregular-shaped microquartz cements (arrows).

small amount of albite (<2%) is also contained in the sandstones. The roundness and sphericity of quartz and K-feldspar grains are variable but larger grains (>400  $\mu\text{m}$  in diameter) show lower roundness and sphericity (<0.3 and <0.4, respectively). In contrast, the roundness and sphericity of chert grains are relatively higher (mostly >0.7 and >0.7, respectively). The sandstones are poorly sorted through the analyzed succession.

Many clastic grains show long to concavo-convex intergranular pressure solution (IPS) textures (arrows in Fig. 3d). Undulose extinction is often recognized in monocrystalline quartz grains (Fig. 3b). Some quartz grains contain apatite ( $\text{Ca}_5(\text{PO}_4)_3\text{Cl}$ ) crystals as inclusion (Figs. 3e and g). These apatite inclusions are monocrystalline and elongated (length close to 30  $\mu\text{m}$ ). Some K-feldspar grains are altered patchily by albite ( $\text{NaAlSi}_3\text{O}_8$ ) (Supplementary Fig. S1). Rounded detrital zircon grains (<200  $\mu\text{m}$  in diameter) are present in the sandstones. The analyzed sandstones also contain small monazite-(Ce) grains (Figs. 3f and h). The grain size of the monazite is mostly <10  $\mu\text{m}$ , and its

particle shape is generally irregular. Monazite grains sometimes aggregate within the intergrain areas. An overgrowth texture is not recognized within a monazite crystal. Our description of the Moodies clastic grains is generally consistent with that in previous studies (Heubeck and Lowe, 1999; Hessler and Lowe, 2006; Heubeck, 2019), in which quartz (70–90%) and K-feldspar (<20%) are major clastic grains in the MdQ1 sandstones in the eastern Saddleback Syncline.

#### 5.1.2. Intergrain areas

Most of the intergrain areas are filled with microquartz and sericite ( $\text{KAl}_2\text{AlSi}_3\text{O}_{10}(\text{OH})_2$ ) (Fig. 4), although micropores (mostly <200  $\mu\text{m}$  in diameter) are also observed in the sandstones throughout the succession. These microquartz and sericite were classified originally into “pseudomatrix” in Heubeck and Lowe (1999). However, we describe them as a cement in this study because their fabrics suggest that they recrystallized from an original matrix (see below and Sections 6 and 7). No original clay matrix is identified clearly in the present sandstones.

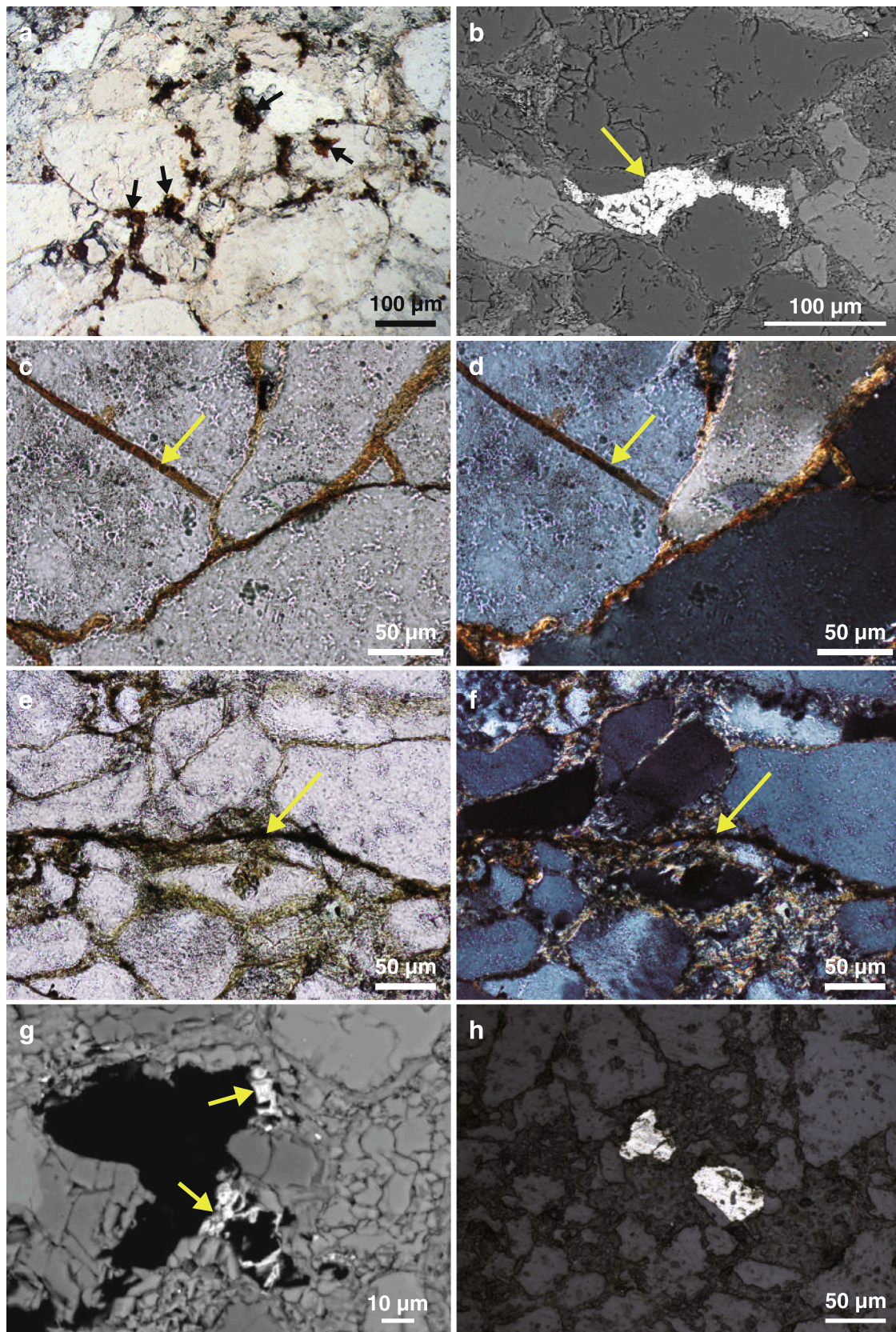


**Fig. 5.** Secondary minerals in the analyzed sandstones. (a) Reddish brown titanium (Ti) oxides (arrows) in grain boundaries (opened nicols). (b) BSE image of Ti oxides (arrow). (c-f) Ti oxide bearing vein (arrow) cutting a quartz grain (c, d) and microquartz-sericite cements (e, f). c and e: opened nicols, d and f: crossed nicols. (g) BSE image of iron oxides (arrows) along a micropore. (h) Pyrite particles (reflected light).

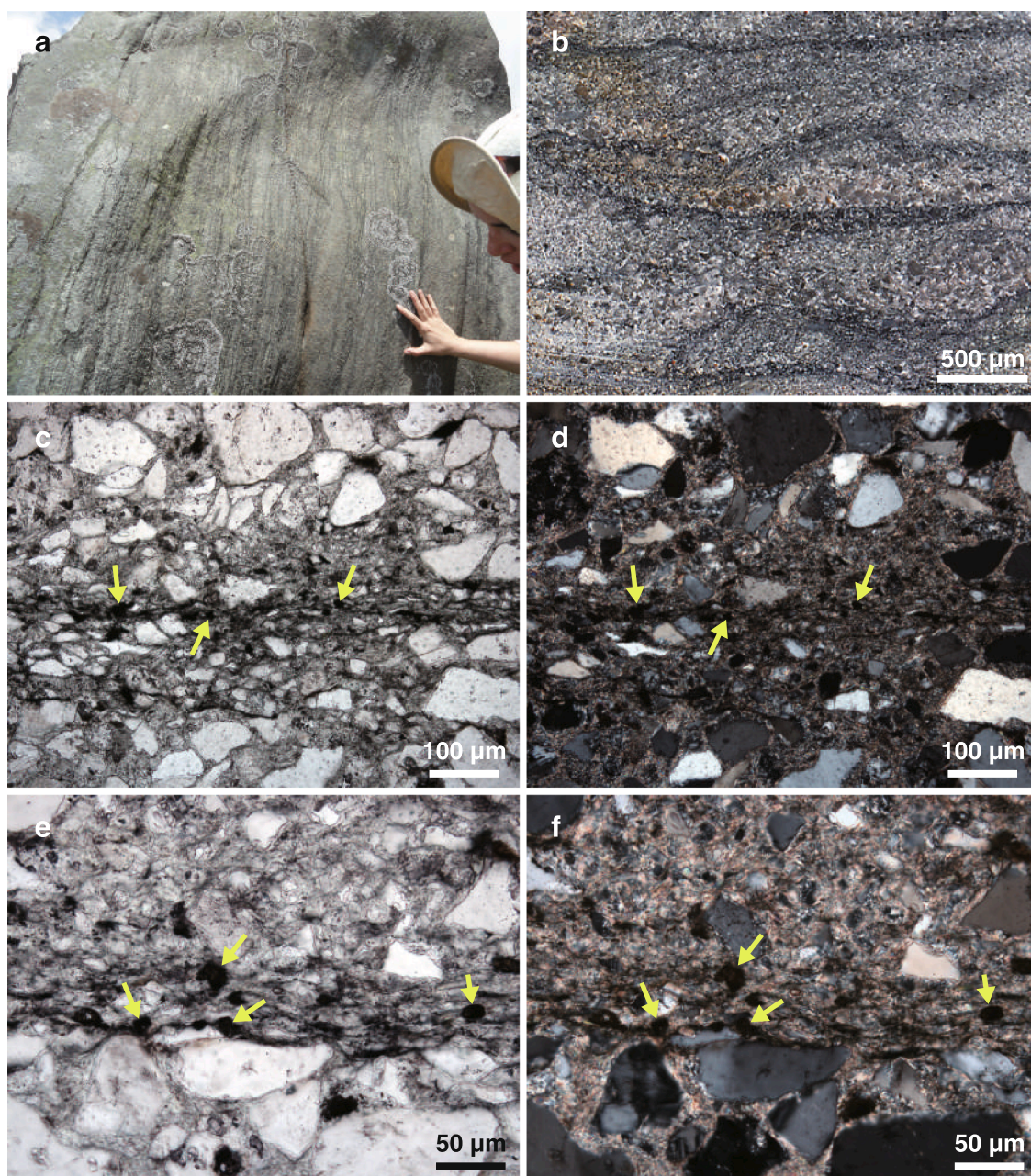


**Fig. 6.** Anastomosing and wavy laminae in the analyzed sandstones. (a, b) Outcrop (a) and slab (b) photos of the laminae. (c, d) A fine-grained microscopic lamina filled with sericite cements. Titanium oxide particles (black dots) are commonly observed within the lamina (arrows). c: opened nicols, d: crossed nicols. (e, f) Ti oxides (arrows) at the boundary between lower coarse-grained sediments and an upper fine-grained lamina. e: opened nicols, f: crossed nicols.

This observation is consistent with the previous interpretation that the original matrix in the Moodies sandstones has been recrystallized totally to a mosaic of fine-grained sericite and microquartz (Heubeck and Lowe, 1999). The microquartz cements fill irregular-shaped spaces between the clastic grains. The sericite cements are also observed around the detrital grains. The sericite crystals are normally elongated up to 30 µm (Fig. 4d). Muscovite is also recognized in the sandstones commonly filling spaces between the clastic grains (Fig. 3e). The size of muscovite crystals is up to 200 µm and their shapes are usually irregular but sometimes subhedral. Some veins filled with sericite cut the microquartz cements and clastic grains (Figs. 4e and f).

Through the analyzed succession, the microquartz cements are generally dominant in the coarser sandstones. In contrast, fine-grained laminae in the subunits 1, 2 and 4 (Fig. 1c), which are frequently intercalated into the coarse sediments, are enriched mostly in sericite

(Figs. 4b and c). The subunit 3 lacks such fine-grained laminae and thus the intergrain areas are filled mainly with microquartz cements (Fig. 4a). In the subunits 1 and 2, the relative proportion of clastic grains to the microquartz and sericite cements is mostly between 40% and 50%. The proportion is higher in the overlying subunit 3 (up to 60%), reflecting the lack of sericite-bearing fine-grained lamina in this subunit. In the uppermost subunit 4, the proportion is between 35% and 50%.

### 5.1.3. Accessory minerals

Various types of oxide mineral are observed in the analyzed sandstones (Fig. 5). Titanium (Ti) oxide particles are common throughout the succession (Fig. 5a). Ti oxides are sometimes observed as aggregates of small (<20 µm) particles. These aggregates are mostly irregular-shaped and sometimes coat clastic grains or fill intergrain areas (Fig. 5b). The Raman results show that the Ti oxides are rutile and anatase. Some veins

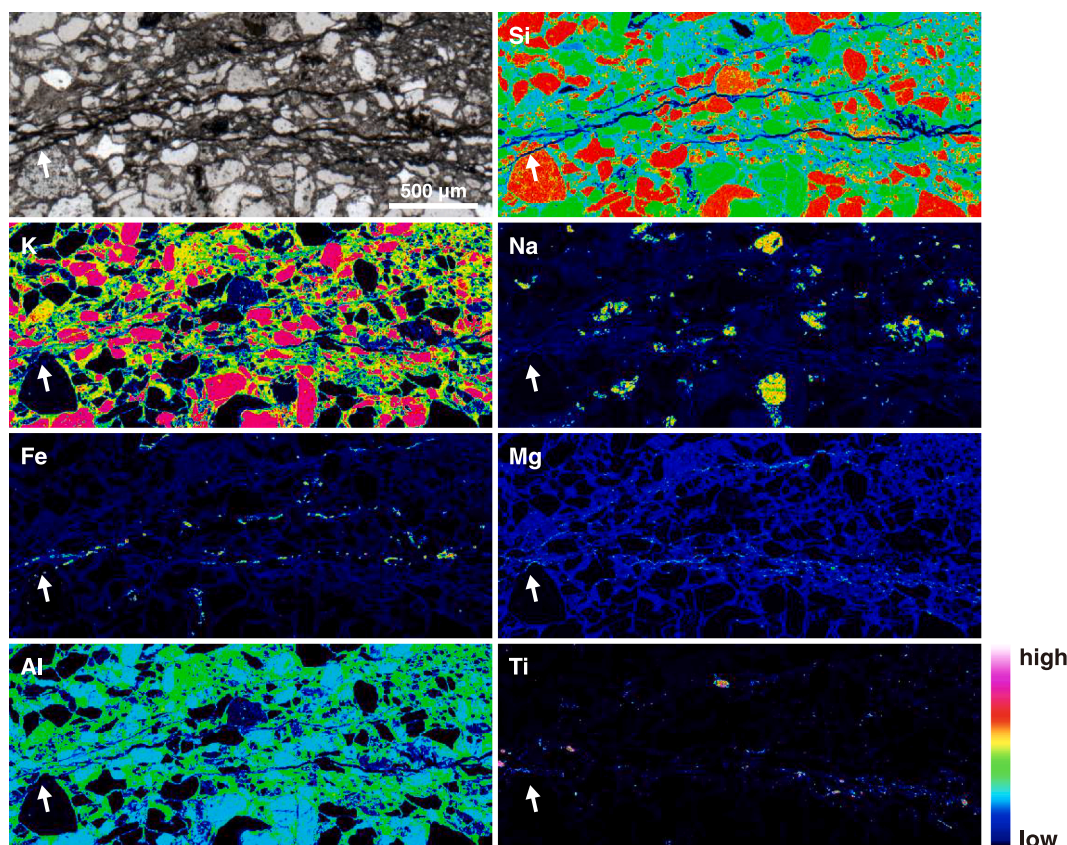


Fig. 7. Photomicrograph (opened nicols) and EPMA maps of a lamina in the subunit 4 of the analyzed succession. The lamina is composed mainly of fine-grained quartz and K-feldspar with Mg-bearing sericite and Fe- and Ti-oxides. Note that a larger chert grain at the lower left corner is cut by the lamina (arrow).

bearing Ti oxides cut both of the microquartz and sericite cements and clastic grains (Figs. 5c–f and 7). Iron (Fe) oxide grains are also recognized in the sandstones. The Fe oxides are irregular shaped and their sizes are mostly  $<50\ \mu\text{m}$ . The Fe oxides are observed within the cements along grain boundaries. Some Fe oxides are also observed along a micropore (Fig. 5g). The Raman results show that some Fe oxides are goethite. The macroscopic LIBS images demonstrate that Fe is mainly concentrated in the secondary altered parts of the sandstones (Supplementary Figs. S2 and S3). The common occurrence of accessory Fe-oxides in the Moodies sandstones is consistent with the previous description in Heubeck and Lowe (1999). Small sulfide grains are also contained in the analyzed sandstones (Fig. 5h) (Saitoh et al., 2020). The sulfides are exclusively pyrite and range in size mostly from 5 to  $100\ \mu\text{m}$ . The shape of the pyrite crystals is mainly irregular but some are euhedral to subhedral. The pyrite crystals are mostly within the cements and along grain boundaries.

#### 5.1.4. Anastomosing and wavy laminae

On the outcrop, anastomosing branching and wavy laminae are frequently observed in the subunits 1, 2 and 4 of the analyzed succession (Figs. 1c, 2c, and 6) (also see log N°9 in Homann et al., 2015). The laminae are dark greenish colored at the hand-specimen scale when observed with the naked eye and are continuous laterally over several to tens of meters. Microscopic observations show that the laminae at the hand-specimen scale correspond to thin (mostly  $<5\ \text{mm}$  thick) and fine-grained laminae intercalated into coarse-grained sandstones (Figs. 2c and 6). Homann et al. (2015) classified these laminae into three morphotypes. They suggested that planar-type laminae are a characteristic of coastal floodplain (subunit 1), whereas wavy-types were typically formed in an intertidal setting (subunit 2). Tufted-types characterized upper inter- to supra-tidal settings (subunit 4). However, we observed frequent planar- and wavy-type laminae in the subunits 1, 2, and 4, and

no tufted-type lamina was observed in the subunit 4. The subunit 3 is characterized by the lack of the anastomosing branching and wavy lamina, as previously observed in Gamper et al. (2011) and Homann et al. (2015).

The laminae are composed of finely fragmented quartz and K-feldspar grains ( $<250\ \mu\text{m}$  in diameter) (Figs. 6 and 7). The intergrain areas in these laminae are composed dominantly of sericite with minor microquartz cements (Figs. 6c–f). Opaque minerals are commonly observed within the laminae and are composed mostly of rutile and anatase and more occasionally of goethite (Fig. 8). Some Ti oxides show an anastomosing microtexture (Figs. 8a and d). In some cases, Ti oxide particles are observed at the boundary between the fine-grained lamina and coarse-grained sediments (Fig. 6e). The Ti concentration within the laminae is confirmed by the EPMA (Fig. 7) and LIBS (Supplementary Figs. S2) images. The LIBS images also show the presence of chromium and boron within the laminae, which are likely incorporated into sericite.

Carbonaceous material occurs scarcely within the anastomosing and wavy laminae in the subunits 1, 2, and 4 (Fig. 1c), as shown by Raman analyses (Figs. 8 and 9). The carbonaceous material was rarely detected, even in laminae, for the seven samples investigated. Only some micrometric regions in one lamina in SAD39 were enriched in carbonaceous material (Fig. 9). Note that the Raman maps are visual representations of a binary matrix, i.e., colored pixels rely on the presence of a given organic/mineral phase, but do not inform on its concentration. In accordance with the previous Raman data in Homann et al. (2018), the detected carbonaceous materials show a Raman signature typical of disordered carbonaceous material that has been submitted to greenschist-facies metamorphism, with an intense and narrow D1 band, a less intense G band, and a D2 band appearing as a shoulder (Figs. 8c and 9f). In the lamina in SAD39, carbonaceous materials occur commonly in association with Ti oxide (rutile and anatase) (Figs. 9c–e):

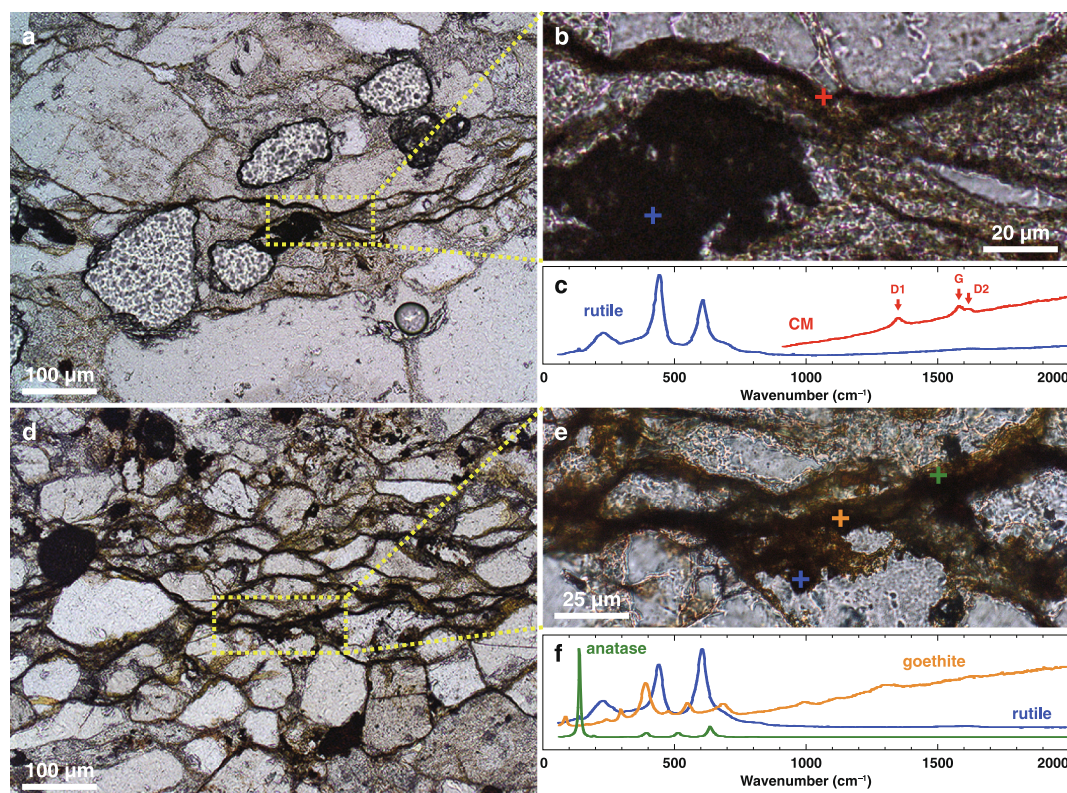


**Fig. 8.** Raman spectra of the analyzed laminae in SAD21 (a-c) and in SAD4 (d-f) in the subunit 1 of the analyzed succession. Flat/wavy laminae at the hand-specimen scale are composed mostly of Ti oxides (rutile and anatase). D1, G, and D2 bands of carbonaceous material (CM) was rarely detected (c) in the laminae for most of the samples investigated. Only some micrometric regions in one lamina in SAD39 are enriched sporadically in CM in the present data set (see Fig. 9).

both of carbonaceous material and Ti oxide are frequently detected at the same spot (Fig. 9f).

## 5.2. Major and trace element geochemistry

Major element diagrams of the analyzed Moodies sandstones are shown in Fig. 10 and Supplementary Fig. S4. All the data are reported in Table 2. The results demonstrate that Si, Al, and K are the three major elements of the analyzed sediments. This is consistent with the microscopic observation that quartz, K-feldspar, and chert clastic grains and microquartz and sericite cements are the major components of the rocks. The SiO<sub>2</sub> contents of the analyzed rocks are mostly between 75 wt% and 95 wt%. The SiO<sub>2</sub> contents of the subunit 3 are higher (>85 wt%) than of other subunits (Fig. 1c), which is consistent with the higher proportion of quartz cement in the intergrain area and the lack of laminae with terrigenous matrix in the subunit (Fig. 10a). Other than that, no major chemical difference is observed in the different subunits. The Na<sub>2</sub>O content of the sample (SAD18) in the subunit 1 is substantially high (>5 wt%, see Table 2) and it is consistent with its extensive albitization observed under microscope. The Al<sub>2</sub>O<sub>3</sub> contents of the sandstones are correlated with the SiO<sub>2</sub> ( $R^2 = 0.97$ ), TiO<sub>2</sub> ( $R^2 = 0.75$ ), K<sub>2</sub>O ( $R^2 = 0.48$ ), and Fe<sub>2</sub>O<sub>3</sub> contents ( $R^2 = 0.44$ ) (Figs. 9a and b and Supplementary Fig. S5) (Table 2). All the subunits share similarly low loss of ignition (LOI) between 0.47 wt% and 2.55 wt% (Fig. 10d). The major element composition of the analyzed sandstones is similar to that of previously analyzed Moodies sandstones (orange circles in Fig. 10). In particular, the present sandstones share the low Fe<sub>2</sub>O<sub>3</sub>, MnO, and MgO contents with the only one sandstone sample from the Saddleback Syncline available in the literature (orange dashed arrows in Fig. 10) (Hessler and Lowe, 2006).

The trace element concentration of the analyzed Saddleback sandstones is reported in Table 3, and their patterns normalized to the upper

continental crust (UCC) are shown in Supplementary Fig. S6. Chondrite- and MuQ-normalized REE patterns are shown in Fig. 11. The trace element patterns of the analyzed sandstones are similar to the modern UCC pattern and show slight depletion in Cs, Nb, Ta, Pb, Sr, V, Co, and Zn and enrichment in Li, Sc, and Cr. The MuQ-normalized patterns show no positive Eu anomaly ( $\text{Eu}/\text{Eu}^* < 1.12$ ). No clear difference is observed between the different subunits in the analyzed succession. The present trace element data are consistent with the previous data of the Moodies sandstones (Hessler and Lowe, 2006).

## 6. Chronology of depositional and post-depositional processes

Based on the petrological descriptions and the geochemical results, we propose a scenario of several processes that have affected the studied Moodies sediments sequentially during and after their deposition (Fig. 12).

### 6.1. Stage 1: Sedimentation

The first stage corresponds to the deposition of detrital grains, mainly quartz, K-feldspars, and chert fragments (Fig. 12a). Quartz and feldspar grains derived mostly from plutonic and felsic volcanic rocks (e.g., Heubeck and Lowe, 1999; Hessler and Lowe, 2006), whereas chert grains were presumably derived from older sedimentary rocks of the Onverwacht and Fig Tree groups (e.g., Heubeck and Lowe, 1999; Saitoh et al., 2020).

The analyzed sediments are subdivided into two types according to their depositional settings. The sediments of the subunit 3 deposited in a subtidal environment (Fig. 1c), in which a constant and high current velocity led to the deposition of coarse grains through large sand bodies (dunes and megaripples, also see Homann et al., 2015). In such a high energy sandy setting, most of fine-grained clay and potential organic

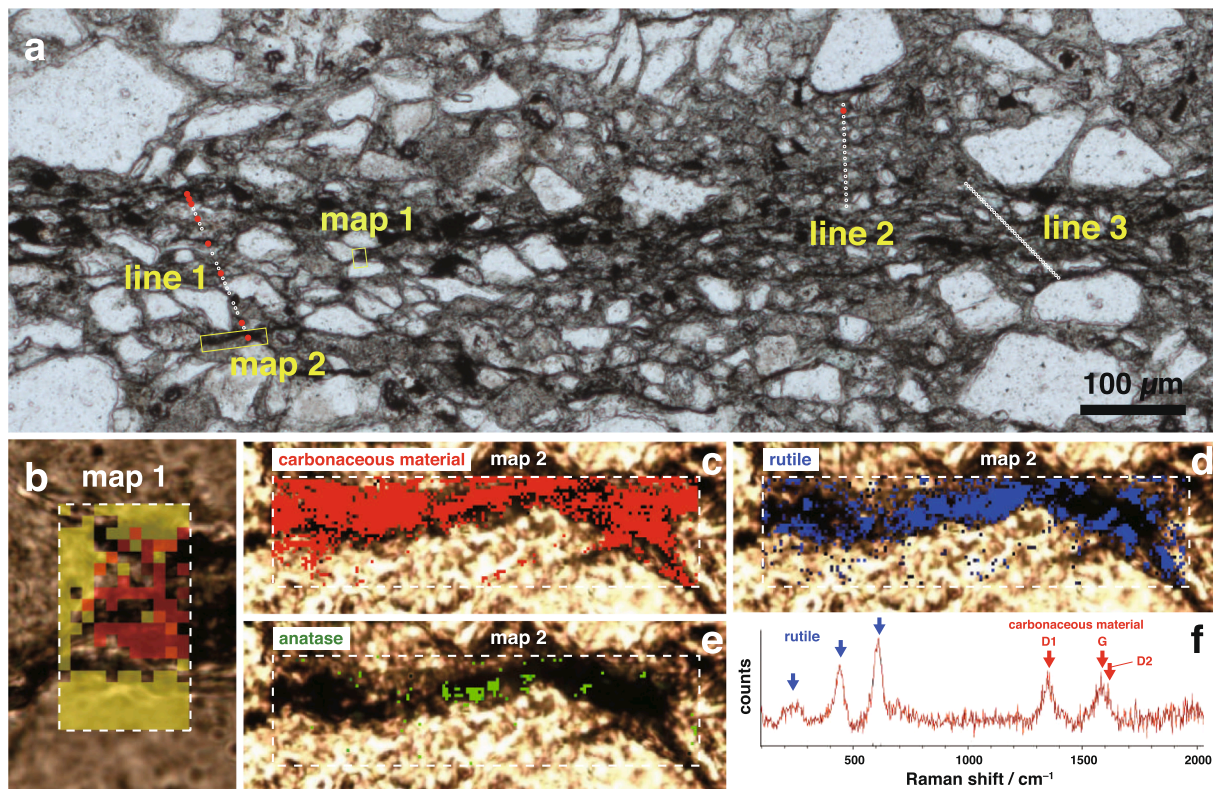


**Fig. 9.** Raman maps on the CM-bearing lamina in SAD39. Note that this is the only lamina enriched sporadically in CM in the present dataset (also shown in Fig. 6c). (a) Microphotograph of the lamina (opened nicols). Lined and mapped regions are shown. On a line, a spot at which CM was detected is shown in red. Note that, even in this lamina, CM exists only sporadically. (b) Raman map 1. CM and K-feldspar are shown in red and yellow, respectively. (c–e) Raman map 2. Note an apparent correspondence between CM and Ti oxide. (f) Raman spectra showing the coexistence of CM and rutile on the map 1. Background fluorescence was subtracted.

matter may have been winnowed and not have accumulated (e.g., Noffke et al., 1997). Accordingly, the  $\text{SiO}_2$  and  $\text{Al}_2\text{O}_3$  contents of samples from the subunit 3 are higher and lower, respectively, than those from other subunits (Fig. 10a). In marked contrast, the sediments of the subunits 1, 2, and 4 deposited in coastal floodplain and inter- to supratidal settings (Fig. 1c) (Homann et al., 2015). These depositional settings were likely characterized by periodical changes in current velocity under the influence of river flush or tides. When the current velocity was temporarily low, relatively fine detrital grains accumulated possibly with a matrix (clay minerals and organic matter), contributing to the formation of a fine-grained lamina intercalated into coarser sediments (Fig. 12a). Although such original clay matrix is not petrographically observed in the present rocks (Figs. 4 and 6), It is commonly recognized in other Moodies localities (e.g., Eriksson and Simpson, 2000; Homann et al., 2018).

In the present sandstones, the supposed presence of the original clay matrix is consistent with the major element geochemistry of the rocks. The  $\text{Al}_2\text{O}_3$  contents are well-correlated with the  $\text{SiO}_2$ ,  $\text{K}_2\text{O}$ ,  $\text{TiO}_2$ , and  $\text{Fe}_2\text{O}_3$  contents (Figs. 10a and b and Supplementary Fig. S5), along a trend with other Moodies shales and sandstones (McLennan and Taylor, 1983; Hessler and Lowe, 2006; Toulkeridis et al., 2015), and igneous clasts in Moodies conglomerates (Sanchez-Garrido et al., 2011; Agangi et al., 2018). These correlations suggest that the major element composition of the initial Moodies sediments was controlled mainly by the relative proportion of quartz and clay matrix, because a similar correlation is commonly observed in modern terrigenous sediments and typically reflects the effect of hydrodynamic sorting of  $\text{Al}_2\text{O}_3$ -,  $\text{K}_2\text{O}$ -,  $\text{Fe}_2\text{O}_3$ -, and  $\text{TiO}_2$ -rich clay from coarse quartz particles in distal and proximal environments (e.g., Singh, 2009). In the subunits 1, 2, and 4 of the present Saddleback succession, more quiescent periods leading to the deposition of fine grains may also have been favorable for potential biofilm installation (e.g., Noffke et al., 1997; Homann et al., 2015).

## 6.2. Stage 2: Microquartz cementation

After the initial sedimentation phase, an interstitial fluid enriched in silica led to microquartz precipitation and cementation between detrital grains in the analyzed Moodies sediments (Fig. 12b). Three potential processes can be considered for the microquartz cementation: 1) low-temperature sediment–water interaction at or below the surface (e.g., Knauth and Lowe, 1978; Lowe, 1999), 2) microquartz precipitation from a hydrothermal fluid (e.g., Knauth and Lowe, 1978; de Wit et al., 1982; Hofmann, 2005; Van Kranendonk, 2006), and 3) IPS and subsequent microquartz cementation during burial (e.g., McBride, 1989; Tada and Siever, 1989).

Our observation suggests that IPS was the main mechanism for the microquartz cementation in the analyzed sediments, for the following reasons. Firstly, the gas-/fluid-escape structures are frequently observed in the analyzed Moodies sandstones (Figs. 2f and g). These structures should have formed in an early diagenetic stage before sediment consolidation (e.g., Lowe, 1975; Homann et al., 2015). The well-preserved and silicified gas-/fluid-escape structures suggest that the microquartz cementation and sediment silicification occurred during burial and are not concomitant with sedimentation (Heubeck, 2019). Microquartz precipitation around the sediment–water interface is therefore unlikely. Secondly, the trace element patterns are similar in all the subunits and show no substantial depletion in mobile elements (Supplementary Fig. S6), implying that the microquartz cementation from an additional hydrothermal fluid was not significant.

Finally, the frequent IPS textures in the analyzed sandstones (Fig. 3d) suggest that the pressure solution during burial contributed substantially to the microquartz cementation. The microquartz cement is commonly observed in the coarser sediments throughout the analyzed succession. It is likely that these coarse sediments were characterized by high intergrain porosity during their deposition in a relatively high-

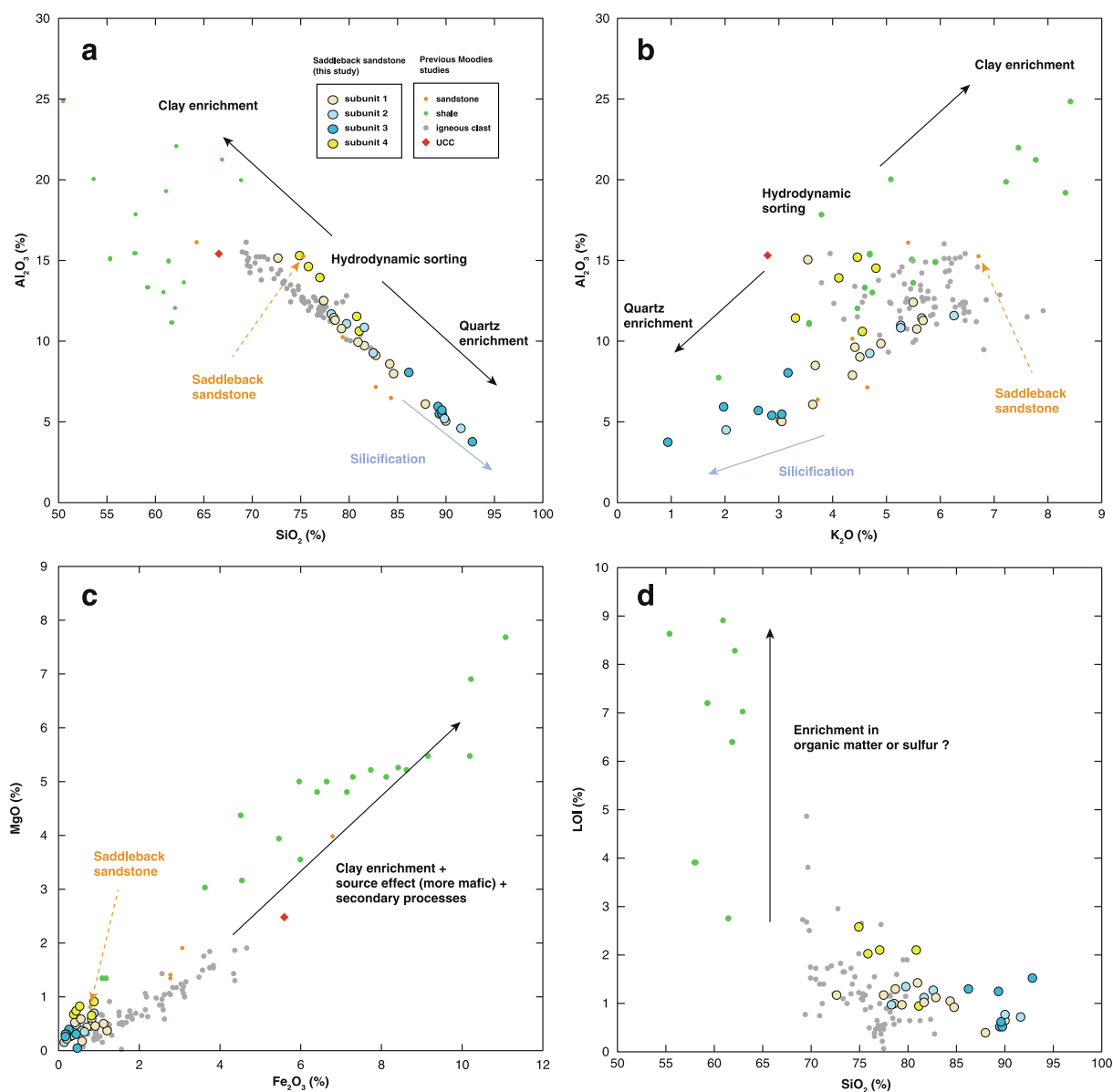


**Fig. 10.**  $\text{SiO}_2$ - $\text{Al}_2\text{O}_3$  (a),  $\text{K}_2\text{O}$ - $\text{Al}_2\text{O}_3$  (b),  $\text{Fe}_2\text{O}_3$ - $\text{MgO}$  (c), and  $\text{SiO}_2$ - $\text{LOI}$  (d) cross plots of the analyzed Moodies succession. Previous sandstone data are from Hessler and Lowe (2006). Shale data are from McLennan and Taylor (1983), Hessler and Lowe (2006), and Toulkeridis et al. (2015). Igneous clast data are from Sanchez-Garrido et al. (2011) and Agangi et al. (2018). The present-day upper continental crust (UCC) composition is from Rudnick and Gao (2014).

energy setting (Stage 1), and were favorable to IPS and silicification during burial diagenesis. The high  $\text{SiO}_2$  contents of coarse sandstones in the subunit 3 ( $>85$  wt%; Fig. 10a) may partly reflect the intense post-depositional silicification, because mineral sorting alone rarely leads to such substantially high  $\text{SiO}_2$  contents (e.g., Singh, 2009). In contrast, the microquartz cement is less present within the fine-grained laminae in the subunits 1, 2, and 4 (Figs. 1c, 4b, and c). The original clay matrix with low porosity likely prevented pervasive microquartz cementation within the laminae.

### 6.3. Stage 3: Sericite cementation

The sericite cements are frequently observed in the analyzed Moodies sediments and are particularly common within the fine-grained laminae in the subunits 1, 2, and 4 (Figs. 1c, 4, and 6c–f). Some sericite veins clearly cut micro-quartz cements (Figs. 4e and f). This geometric relationship implies that the sericite cementation occurred after the sediment silicification and consolidation (Stage 2). We interpret that

the original clay matrix within the fine-grained laminae (Stage 1) was replaced with sericite by a fluid circulation along the bedding during later metasomatism (Fig. 12c).

The major and trace element geochemistry of the analyzed Moodies sandstones does not show a typical feature of sediments being flushed at high temperature with high water/rock ratios (Figs. 10 and 11 and Supplementary Fig. S6) (e.g., bell-shape in the REE pattern and depletion in moderately immobile elements; McLennan, 1989). This suggests that the sericite cementation was not due to a hydrothermal fluid circulation. Rather, the major and trace element composition of the analyzed sandstones is similar to that of their potential sources (i.e., igneous clasts in the Moodies; Agangi et al., 2018). It indicates that secondary processes were not intense enough to leach out less-mobile elements and to erase the geochemical information about the provenance of the sediments (Hessler and Lowe, 2006). The analyzed Moodies sandstones have not been altered substantially by a hydrothermal fluid. We thus infer that the sericite cementation occurred during metasomatism, with a relatively low-temperature fluid, that has been

**Table 2**  
Major element data. L.O.I: loss of ignition.

Sample ID	Subunit	Thickness m	Depositional setting	SiO <sub>2</sub> %	Al <sub>2</sub> O <sub>3</sub> %	Fe <sub>2</sub> O <sub>3</sub> tot %	MgO %	CaO %	Na <sub>2</sub> O %	K <sub>2</sub> O %	TiO <sub>2</sub> %	MnO %	P <sub>2</sub> O <sub>5</sub> %	L.O.I. %	Total %
SAD 39	4	341.0	upper inter to supratidal	81.2	10.6	0.4	0.6	0.2	0.5	4.6	0.3	0.0	0.1	0.9	99.4
SAD 38	4	330.0	upper inter to supratidal	81.0	11.4	0.5	0.7	0.1	0.0	3.3	0.3	0.0	0.1	2.1	99.5
SAD 37	4	322.0	upper inter to supratidal	76.0	14.5	0.9	0.9	0.1	0.0	4.8	0.5	0.0	0.1	2.0	99.8
SAD 36	4	321.0	upper inter to supratidal	75.1	15.2	0.9	0.6	0.0	0.0	4.5	0.6	0.0	0.0	2.5	99.5
SAD 35	4	320.0	upper inter to supratidal	77.2	13.9	0.6	0.8	0.1	0.1	4.1	0.4	0.0	0.1	2.1	99.3
SAD 34	3	312.0	subtidal	92.9	3.7	0.5	0.0	0.0	0.0	1.0	0.0	0.0	0.0	1.5	99.7
SAD 33	3	290.0	subtidal	89.3	5.9	0.3	0.4	0.1	0.1	2.0	0.1	0.0	0.0	1.2	99.5
SAD 32	3	276.0	subtidal	89.5	5.4	0.2	0.3	0.1	0.1	3.1	0.1	0.0	0.0	0.5	99.3
SAD 31	3	259.0	subtidal	89.8	5.4	0.2	0.2	0.0	0.1	2.9	0.1	0.0	0.0	0.5	99.4
SAD 30	3	253.0	subtidal	89.7	5.7	0.3	0.3	0.0	0.1	2.7	0.1	0.0	0.0	0.6	99.5
SAD 29	3	247.0	subtidal	86.3	8.0	0.5	0.3	0.0	0.1	3.2	0.2	0.0	0.0	1.3	99.9
SAD 27	2	233.0	intertidal	79.9	11.0	0.9	0.7	0.1	0.1	5.3	0.4	0.0	0.1	1.3	99.8
SAD 26	2	232.0	intertidal	81.8	10.8	0.5	0.4	0.0	0.1	5.3	0.4	0.0	0.0	1.1	100.3
SAD 25	2	217.0	intertidal	90.1	5.1	0.2	0.1	0.0	0.0	3.1	0.1	0.0	0.0	0.7	99.4
SAD 24	2	214.0	intertidal	91.7	4.5	0.3	0.2	0.0	0.1	2.0	0.2	0.0	0.0	0.7	99.9
SAD 23	2	206.0	intertidal	82.8	9.2	0.7	0.3	0.0	0.2	4.7	0.3	0.0	0.0	1.2	99.5
SAD 22	2	198.0	intertidal	78.4	11.6	0.5	0.5	0.0	0.6	6.3	0.3	0.0	0.0	1.0	99.1
SAD 21	1	197.5	coastal floodplain	78.7	11.4	0.9	0.6	0.1	0.4	5.7	0.5	0.0	0.1	1.0	99.2
SAD 20	1	155.0	coastal floodplain	84.4	8.5	0.4	0.5	0.1	0.3	3.7	0.3	0.0	0.0	1.0	99.3
SAD 19	1	134.0	coastal floodplain	84.8	7.9	0.4	0.3	0.0	0.5	4.4	0.2	0.0	0.0	0.9	99.4
SAD 18	1	131.0	coastal floodplain	72.8	15.1	1.2	0.3	0.1	5.3	3.6	0.3	0.0	0.1	1.1	99.9
SAD 13	1	51.0	coastal floodplain	83.0	9.0	0.9	0.4	0.0	0.3	4.5	0.4	0.0	0.0	1.1	99.8
SAD 9	1	18.0	coastal floodplain	81.8	9.6	1.2	0.5	0.1	0.1	4.4	0.4	0.0	0.1	1.0	99.1
SAD 8	1	17.0	coastal floodplain	77.6	12.4	0.6	0.6	0.0	0.6	5.5	0.5	0.0	0.1	1.1	99.1
SAD 7	1	11.5	coastal floodplain	81.1	9.8	0.8	0.4	0.0	0.4	4.9	0.4	0.0	0.1	1.4	99.3
SAD 5	1	6.5	coastal floodplain	88.1	6.0	0.3	0.2	0.0	0.7	3.7	0.1	0.0	0.0	0.4	99.4
SAD 4	1	6.0	coastal floodplain	78.8	11.2	0.8	0.4	0.0	0.8	5.7	0.5	0.0	0.0	1.3	99.5
SAD 3	1	2.5	coastal floodplain	79.4	10.7	0.6	0.4	0.0	1.0	5.6	0.4	0.0	0.1	1.0	99.1
SAD 1	1	1.5	coastal floodplain	90.2	5.0	0.6	0.2	0.0	0.3	3.1	0.2	0.0	0.0	0.6	100.2

commonly observed in the entire BGB rocks (e.g., [Condie et al., 1977](#); [de Ronde and de Wit, 1994](#); [Hofmann, 2005](#)), including the Moodies Group (e.g., [Heubeck and Lowe, 1999](#); [Heubeck, 2019](#)). The present geochemical data suggest that the original clay matrix in the laminae was replaced with sericite during low-grade and fluid mediated metamorphism ([Dunoyer de Segonzac, 1970](#); [Heubeck, 2019](#)).

#### 6.4. Stage 4: Ti oxide formation

Ti oxides (rutile and anatase) are common in the analyzed sandstones ([Fig. 5a](#)). They form aggregates of small (<20 µm) particles, coat clastic grains, fill irregular-shaped intergrain areas, and represent anastomosing textures ([Figs. 5b and 8](#)). The dark and microscopic Ti-oxide laminae follow parallel to the bedding and are present mainly in the fine-grained sericite-rich laminae. Also, some veins bearing Ti oxides cut both of clastic grains and microquartz and sericite cements ([Figs. 5c–f](#)). All these textures indicate that the Ti oxides formed secondarily after the microquartz and sericite cementation (Stage 2 and Stage 3, respectively) ([Fig. 12d](#)). The Ti oxides can commonly form during diagenesis and low-grade metamorphism via recrystallization of Ti-bearing minerals like ilmenite, biotite and feldspars (e.g., [Richards et al., 1988](#); [Smith et al., 2009](#); [Bower, 2011](#); [Galvez et al., 2012](#)). Ti is highly stable and insoluble in a fluid (e.g., [Brookins, 1988](#)), though it can be more mobile in the presence of phosphate ions ([Pe-Piper et al., 2011](#)). Our observations suggest that the Ti oxides formed via the reaction of Ti-bearing detrital grains during metamorphism ([Figs. 12a and d](#)).

A close association of carbonaceous material and Ti oxide in sedimentary rocks has been reported ([Foucher et al., 2012](#); [Galvez et al., 2012](#); [Lekele Baghekema et al., 2017](#); [Sirantoine et al., 2020](#)), even in fossilized microbial mats ([Noffke et al., 2008](#)). Although the carbonaceous material has been observed only in the laminae that contain Ti oxides in the present sandstones ([Figs. 8 and 9](#)), the general scarcity of carbonaceous material through the analyzed succession does not allow us to conclude firmly on the systematic association of carbonaceous material with Ti oxide. The origin of this apparent association is still

unknown and various processes have been suggested for it from biological accumulation to post-depositional and diagenetic mobilization ([Glamoclija et al., 2009](#); [Sirantoine et al., 2020](#)).

#### 6.5. Stage 5: Rainwater infiltration

Finally, Fe oxides precipitated during a recent oxic rainwater infiltration into the analyzed Moodies sediments ([Fig. 12e](#)) ([Heubeck, 2019](#)). The Fe oxides are irregular shaped and observed within the cements along grain boundaries and rarely within a fine-grained lamina. Some Fe oxides are observed along a micropore ([Fig. 5g](#)). The occurrence of Fe oxide along a micropore is consistent with the rainwater infiltration scenario into the sediments. The macroscopic LIBS images also suggest that Fe is concentrated mainly in the reddish-brown superficially altered parts and that its distribution is unrelated to the bedding in the analyzed sandstones ([Supplementary Figs. S2 and S3](#)). A plausible Fe source for the oxides is pyrite crystals in the sandstones ([Saitoh et al., 2020](#)). Although the timing of the rainwater infiltration and Fe oxide formation is poorly constrained, [Heubeck \(2019\)](#) suggested that they occurred very recently. It is apparently consistent with the work by [Bonnand et al. \(2020\)](#), showing that the emplacement of the negative Ce anomalies of the Moodies BIF samples occurred in the last 100 Ma.

#### 6.6. Correspondence to the regional thermal history

During the Moodies deposition, the emplacement of several plutonic domains occurred around the BGB at 3.23–3.21 Ga ([Fig. 1a](#)) (e.g., [de Ronde and de Wit, 1994](#)), including the Kaap Valley Pluton at ~3.21 Ga (e.g., [Moyen et al., 2019](#) and references therein) and the Archean Gneiss Complex (AGC) at 3.24–3.07 Ga (e.g., [Taylor et al., 2012](#); [Kröner et al., 2018](#); [Wang et al., 2020](#)), associated with the major D2 deformation event in the BGB (e.g., [de Ronde and de Wit, 1994](#)). The 3.23–3.21 Ga emplacement was followed by major tectono-thermal events at ~3.1, ~2.7, and ~2.1 Ga ([Weis and Wasserburg, 1987](#); [de Ronde et al., 1991a](#); [Lécuyer et al., 1994](#); [Toulkeridis et al., 1994, 1998](#)). The extensive emplacement of the large plutons of the granodiorite-monzogranite-

**Table 3**  
Trace element data.

Sample ID	Subunit	Thickness (m)	Depositional setting	Cs	Rb	Ba	Th	U	Nb	Ta	La	Ce	Pr	Pb	Nd	Sr	Sm	Zr	Hf	Eu	Gd	Tb	Dy	Ho	Y	Er	Li	Yb	Lu	Sc	V	Cr	Co	Ni	Cu	Zn	Ga
SAD 39 4	341.0	upper inter to supratidal	2.6	122.1	571.0	12.4	1.5	8.1	0.9	21.2	46.7	5.0	17.0	16.5	78.1	2.8	164.2	4.2	0.6	2.0	0.3	1.6	0.3	8.3	0.9	8.2	1.0	0.1	4.0	23.3	261.3	0.5	7.0	3.6	0.3	11.9	
SAD 37 4	322.0	upper inter to supratidal	4.0	128.9	464.4	24.1	3.0	10.2	1.2	81.3	136.1	13.1	12.8	43.8	49.3	6.7	246.6	6.4	1.2	4.9	0.7	3.7	0.7	19.9	2.1	6.7	2.1	0.3	7.2	39.1	519.2	1.0	16.8	4.0	0.8	18.8	
SAD 32 3	276.0	subtidal	1.5	74.8	491.3	2.8	0.7	1.3	0.2	14.9	25.7	2.6	10.9	8.6	48.6	1.3	45.3	1.3	0.3	1.1	0.2	1.0	0.2	5.8	0.6	1.5	0.6	0.1	1.2	6.5	32.0	0.4	3.2	3.0	-1.2	6.0	
SAD 29 3	247.0	subtidal	2.1	87.4	302.1	16.9	1.6	6.1	0.7	70.0	132.3	12.8	9.6	41.1	31.8	5.8	142.5	3.6	0.9	3.7	0.5	2.4	0.4	11.9	1.3	7.2	1.4	0.2	3.6	20.0	283.1	0.5	3.6	5.8	-0.4	13.3	
SAD 27 2	233.0	intertidal	2.7	133.2	503.3	20.6	5.6	9.3	1.0	37.1	78.1	8.0	16.4	27.5	65.6	4.8	217.9	5.4	1.0	4.0	0.6	3.2	0.6	17.7	1.8	12.5	1.7	0.2	5.6	31.1	482.9	8.7	37.6	15.0	4.1	13.9	
SAD 24 2	214.0	intertidal	1.2	48.3	227.9	9.8	1.5	3.4	0.5	64.1	123.2	12.1	18.4	39.2	65.2	5.4	60.8	1.7	0.9	3.0	0.4	1.7	0.3	8.4	0.9	4.6	0.9	0.1	2.6	14.8	90.7	0.5	8.1	5.7	-1.6	9.9	
SAD 22 2	198.0	intertidal	3.5	143.9	611.1	12.7	1.8	8.1	0.9	42.3	86.3	8.5	14.3	27.7	80.1	4.2	154.6	3.9	0.9	3.0	0.4	2.2	0.4	11.9	1.3	20.8	1.3	0.2	4.8	27.1	255.6	0.6	5.6	3.8	0.9	15.7	
SAD 19 1	134.0	coastal	2.2	94.1	517.9	13.0	1.6	5.2	0.6	34.8	68.5	6.7	14.4	21.8	62.8	3.1	131.9	3.4	0.6	2.1	0.3	1.8	0.4	10.2	1.1	8.6	1.2	0.2	3.2	18.1	154.8	0.4	8.8	4.9	3.5	9.9	
SAD 18 1	131.0	floodplain	2.1	77.9	340.9	7.7	2.3	8.7	0.9	18.5	37.1	4.2	19.2	15.6	263.9	3.1	166.6	4.3	0.7	2.6	0.4	2.1	0.4	12.2	1.3	9.2	1.3	0.2	4.2	24.2	14.5	3.2	77.2	21.3	5.2	17.5	
SAD 5 1	6.5	floodplain	1.8	76.0	449.1	4.7	0.8	2.5	0.3	21.3	40.6	4.1	12.7	13.0	52.6	1.9	53.7	1.5	0.4	1.5	0.2	1.4	0.3	7.7	0.8	6.7	0.8	0.1	1.7	9.5	67.3	1.5	16.0	5.1	173.0	6.8	
SAD 3 1	2.5	floodplain	2.5	121.3	617.0	15.0	2.6	8.5	1.0	53.9	104.6	10.7	12.1	36.2	82.5	5.6	217.6	5.5	1.0	3.5	0.4	2.2	0.4	11.7	1.3	8.7	1.3	0.2	5.7	41.4	405.3	0.9	13.1	12.1	0.4	15.4	

syenite (GMS) occurred at ~3.1 Ga (beige colored areas in Fig. 1a) (e.g., Anhaeusser et al., 1981). The wide distribution of this event indicates that the BGB sediments, including the Moodies, were substantially affected by associated heating. There are a number of gold deposits in the northern central BGB, some in close proximity (<10 km) to the analyzed Saddleback section (Munyai et al., 2011; Selvaraja et al., 2017). These gold deposits formed at ~3.1–3.0 Ga based on rutile and titanite U-Pb ages (de Ronde et al., 1991a, 1992; Agangi et al., 2019), presumably in association with the GMS event. This age is identical to the Sm-Nd age of carbonate-derived clay minerals in the Fig Tree Group in the central BGB (Toulkeridis et al., 1994), supporting the large influence of the GMS emplacement on the BGB sediments. Another major thermal event occurred widely in the BGB at ~2.7 Ga (e.g., de Ronde et al., 1991b; Toulkeridis et al., 1998). Toulkeridis et al. (1998) suggested extensive silicification and sericitization of carbonates in the Onverwacht and Fig Tree groups by low-temperature fluids (~200 °C) at ~2.7 Ga, resetting the Pb-Pb, Sm-Nd, and Rb-Sr isotopic systems. The ~2.7 Ga thermal event was followed by a later one widespread in the BGB at ~2.1 Ga, based on Rb-Sr, Sm-Nd, and <sup>40</sup>Ar/<sup>39</sup>Ar dating of the Onverwacht and Fig Tree sediments (e.g., Weis and Wasserburg, 1987, de Ronde et al., 1991b).

The present Moodies sandstones in the central BGB were presumably affected by all these polymetamorphism/tectono-thermal events (e.g., Heubeck and Lowe, 1999). Previously published Raman temperature estimates on Moodies carbonaceous materials provided temperature ranging between 350 °C and 375 °C (Nabhan et al., 2017; Homann et al., 2018; Kohler and Heubeck, 2019). If the microquartz cements formed during burial diagenesis, the sericite cementation (Stage 3; Fig. 12c) and Ti oxide formation (Stage 4; Fig. 12d) in the analyzed Moodies sandstones could correspond to any of the multiple tectono-thermal events that occurred at a regional scale between ~3.1 Ga and ~2.1 Ga.

### 7. Origin of the analyzed Moodies anastomosing and wavy laminae

Noffke et al. (2006) were the first to propose the presence of various types of MISS (e.g., wrinkle and roll-up structures) in the Moodies sediments from the Dycedale and Saddleback synclines. Later studies generalized the presence of fossilized microbial mats in the Moodies sediments as anastomosing and wavy laminae (Heubeck, 2009, 2019; Homann et al., 2015, 2018; Homann, 2019; Köhler and Heubeck, 2019). Specific ecological and taphonomic conditions are generally required for the formation and preservation of microbial mats in ancient sandstones (Noffke et al., 2001). Along the different Moodies successions in the Saddleback Syncline, Homann et al. (2015) argued in favor of morphological adaptation of microbial mats (planar-, wavy-, and tufted-types) to the different paleoenvironments (coastal, intertidal, and inter- to supratidal settings, respectively). Unfortunately, we have not been able to reproduce such a correlation between mat morphology and depositional setting along the studied section. The identification of structures morphologically similar to microbial mats in Moodies fluvial conglomerates also led some authors to conclude the existence of a Paleoproterozoic terrestrial biosphere (Homann et al., 2018). The presence and preservation of biofilms or anastomosing and wavy laminae in the Moodies sediments thus seem to occur in various depositional settings (Homann, 2019).

Some Moodies environments are nevertheless characterized by the absence of such laminae as seen in the subunit 3 of the Saddleback Syncline succession. The sediments of this subunit accumulated in a relatively shallow subtidal setting, characterized by strong tidal currents and storms (Homann et al., 2015). Under such consistently high-energy conditions, putative biofilms or a matrix with organic matter would be likely reworked and vanished (Gerdes et al., 2000; Noffke et al., 2003). In contrast, coastal floodplain and supra- to inter-tidal settings under fluctuating energy conditions, corresponding to the present subunits 1, 2, and 4, are known to be more suitable for the biomat formation and

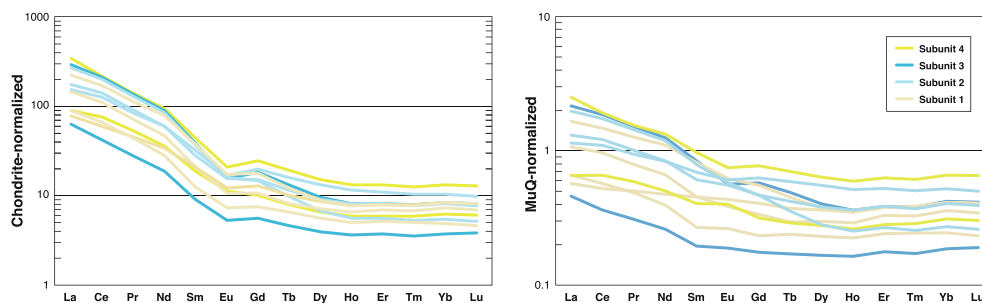


Fig. 11. Chondrite- and MuQ-normalized REE patterns of the four subunits of the analyzed succession. Note that the REE patterns are generally consistent through the succession and no clear Eu anomaly is recognized on the MuQ-normalized patterns.

preservation (e.g., Noffke et al., 1997; Noffke, 2010; Newman et al., 2017). In these latter subunits, the laminae are relatively continuous laterally over several to tens of meters and are present stratigraphically almost every centimeter over a >200-m-thick succession. Archean to modern examples of MISS that developed in tidal environments indicate that, even when microbial biofilms can tolerate high energy events, their installation and development require a period of no sediment accumulation under quiet conditions (e.g., Gerdes and Klenke, 2007; Eriksson and Wilde, 2010; Noffke, 2010; Cuadrado et al., 2013). Such ecologic and taphonomic windows of microbial mat development and preservation (also see Noffke, 2009) appear questionable in the light of the rather tight and continuous record of anastomosing and wavy laminae, with little evidence for tearing and transportation of biofilm fragment, along the analyzed Moodies succession.

Based on the present results, we reinterpret the formation of the anastomosing and wavy laminae observed along the studied succession in the Saddleback Syncline, previously suggested to be ancient microbial mats (Homann et al., 2015) (Fig. 12). Our petrological observations show that these laminae are composed mainly of fine grains with secondary sericite and Ti oxide (Figs. 6, 8, and 12), and are aligned with the bedding and sometimes crosscut detrital grains and microquartz cements that formed during diagenetic burial (Fig. 7). These observations suggest a strong contribution of post-burial metasomatic fluid flow to the lamina during Mesoproterozoic to Paleoproterozoic tectono-thermal events (Fig. 12c). Moreover, the multiple sulfur isotope records of pyrite indicate the secondary addition of hydrothermal sulfur to the analyzed sandstones possibly via fluid injections (Saitoh et al., 2020). Nonetheless, the major and trace element compositions of these sandstones are not depleted in moderately immobile elements, and the MuQ-normalized REE patterns show no positive Eu anomaly (Fig. 11). These geochemical data do not support an extensive hydrothermal fluid circulation, but suggests that the fluids were rather endogenous and circulated only within the sedimentary unit. The observed Moodies anastomosing and wavy laminae are thus closely associated with low-grade fluid-mediated metamorphic events (Fig. 12). Similar dark laminated textures with a mineral assemblage including Ti oxide were previously described in younger 2.9 Ga sandstones of the Pongola Supergroup in Bower (2011), and were interpreted to be formed as a result of the circulation of low-grade metamorphic fluids. The author precisely warned the community about the risk to misinterpret lamination with such mineral assemblage as ancient microbial mats.

Microscopic dark laminae from the same Moodies succession were previously referred as “kerogenous” (Homann et al., 2015). However, carbonaceous matter was rarely identified in our Raman analyses (Figs. 8 and 9). Our results demonstrate that not all wavy anastomosing laminae in the Moodies rocks are kerogenous. Raman spectroscopy does not provide quantitative estimation of the amount of carbonaceous matter and sufficient chemical information to identify disordered carbonaceous matter as kerogen (Pasteris and Wopenka, 2003). However, both of the present and previous studies reported the substantially low LOI (<2.55 wt%) and TOC contents (<1000 ppm) in the Moodies

sandstones (Tables 2 and S2; Homann et al. 2018). It is worth noting that the lamina-bearing subunits 1 and 4 do not show any TOC enrichment compared to the subunit 3 (devoid of anastomosing and wavy lamination), suggesting that carbonaceous material is homogeneously scarce in the studied Moodies sandstones (Table S2). Nonetheless, we emphasize that the present results do not demonstrate that organic matter was ordinarily scarce in the Moodies laminae in the subunits 1, 2, and 4 during the sediment accumulation. Rather, it is likely that the observed fine-grained laminae primarily contained some organic matter in the analyzed Moodies sediments (Stage 1) (Fig. 12a). However, due to the substantial secondary overprints during the long post-depositional history (Fig. 12), it is difficult to determine whether the rarely detected carbonaceous materials in the laminae are a remnant of original microbial mats or of sedimentary organic matter, which had been incorporated into the fine-grained laminae during the sediment accumulation. In the analyzed Moodies sandstones, intense silica precipitation that occurred mainly in the coarse-grained sediments after burial (Stage 2) may have prevented, at least in part, organic remains from escaping from the sediments during burial (Fig. 12b). Indeed, the entombment of microorganisms into silica significantly limits their molecular degradation during experimental diagenesis (Alleon et al., 2016; Igisu et al., 2018). Spatially resolved studies of organic microstructures in similarly metamorphosed Paleoproterozoic cherts have consistently documented their chemical preservation with both geochemical and petrographic evidence against organic migration from the microstructures (e.g., van Zuilen et al., 2007; Westall et al., 2011; Alleon et al., 2018, 2021; Hickman-Lewis et al., 2020). On the other hand, later metasomatism (Stage 3) and a recent oxidative weathering event (Stage 5) may have participated to leach carbonaceous matter from the Moodies sediments (Petsch et al., 2000).

The occurrence of carbonaceous material in the Moodies sandstones has been reported in several other localities in the central Saddleback Syncline (Gamper et al., 2011) and in the Stolzburg and Dycedale synclines (Noffke et al., 2006; Nabhan et al., 2017; Homann et al., 2018; Köhler and Heubeck, 2019), and has been associated with the morphology of anastomosing and wavy laminae interpreted as a remnant of original microbial mats. However, based on the present petrological and geochemical observations, the anastomosing and wavy laminations frequently observed in the studied Moodies sandstones are not necessarily consistent with the existence of original microbial mats. Our results also emphasize that the Moodies sediments are substantially different from cherts from the older Onverwacht and Fig Tree groups that contain substantial amounts of organic matter (e.g., Hofmann and Bolhar, 2007; Van Zuilen et al., 2007; Hofmann et al., 2013; Marin-Carbonne et al., 2018; Alleon et al., 2021). In the future, research on new sedimentary successions and rock samples would advance our understanding of traces of life preserved in the Moodies sediments, especially in the framework of the upcoming BASE ICDP drilling project, although it will be important to bear in mind the secondary overprint of metasomatism on the Moodies laminae.

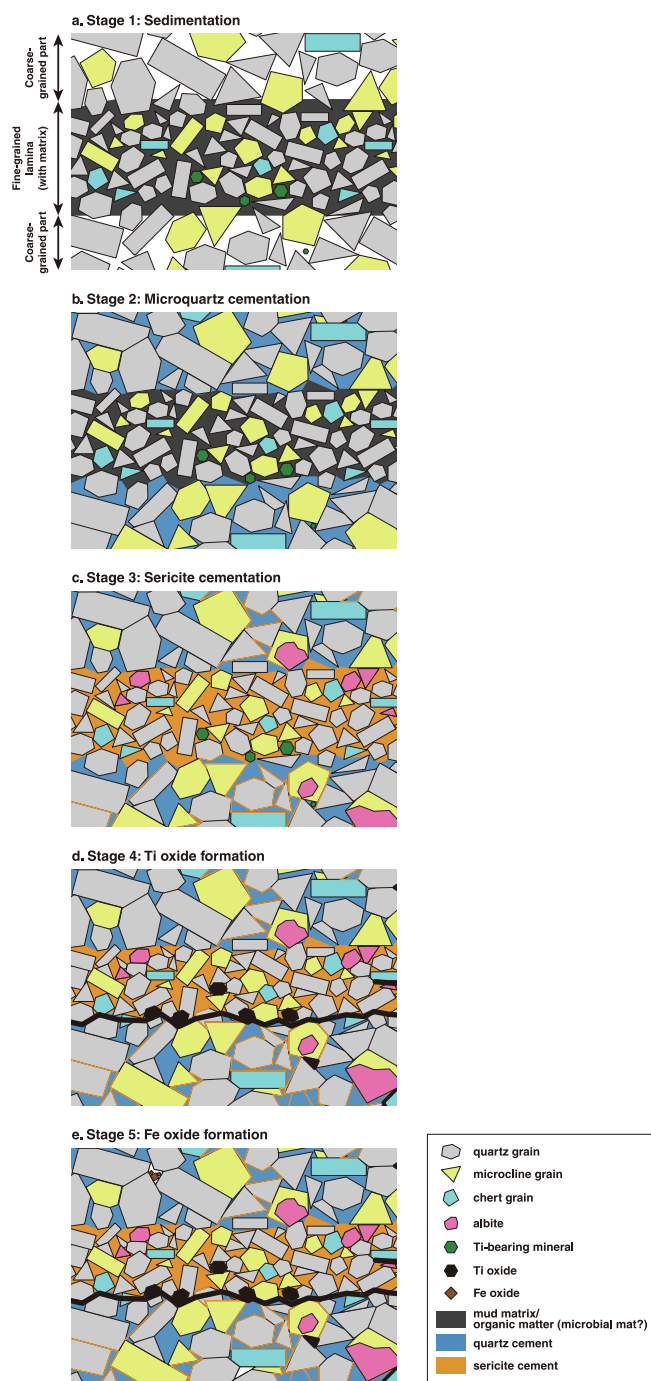


Fig. 12. Schematic model for the depositional and post-depositional history of the analyzed Moodies sandstones.

## 8. Conclusions

The quartz-rich sandstones of the 3.22 Ga Moodies Group were collected from a ~350 m thick succession in the Saddleback Syncline in the central Barberton Greenstone Belt, South Africa. Petrological and multiple geochemical characteristics of the rocks were analyzed to reconstruct their post-depositional history and to examine the origin of anastomosing and wavy laminae in the rocks, which were previously suggested to be a remnant of microbial mats. The laminae are frequently observed in coastal floodplain and inter- to supra-tidal settings, but not in a consistently high-energy subtidal setting, in the analyzed succession. Our results show that, after an initial phase of sedimentation (Stage

1), the studied sandstones have been affected by complex post-depositional processes, including at least three main processes with four post-depositional stages: (i) intergranular pressure solution leading to the microquartz cementation during the diagenesis burial (Stage 2); (ii) formation of a sericite cement (Stage 3) and Ti oxide (Stage 4) during low-grade and fluid mediated metamorphism; and (iii) rainwater infiltration that triggered more recent precipitation of Fe oxide (Stage 5). This post-depositional history appears strongly dependent on the paleo-environment and nature of the sediments. In high energy settings, coarse-grained sediments characterized by an intergrain porosity allowed the microquartz cementation, which prevented the coarse sediments from later fluid injections. In contrast, under fluctuating energy settings, periods of more quiescent hydrodynamic conditions allowed the repeated deposition of fine-grained laminae with a clay matrix. This original matrix, which prevented the fine-grained laminae from the microquartz cementation, was later replaced with sericite. Although we do not exclude that some of the observed Moodies laminae were originally microbial mats, the mineral assemblage of the studied anastomosing and wavy laminae (i.e., mainly sericite associated with Ti oxide and rare carbonaceous material) shows a substantial metamorphic overprint, implying that similar laminae cannot be unambiguously associated with the concept of a flourishing Paleoproterozoic microbial life at 3.22 Ga.

## Declaration of Competing Interest

The authors declare that they have no known competing financial interests or personal relationships that could have appeared to influence the work reported in this paper.

## Acknowledgements

We thank Christoph Heubeck, Martin Homann, Phillip Andreas Zametzer and Deon Janse van Rensburg for their assistance with locating the sampling section and for fruitful discussions. Moritz Mühlberg assisted with the sampling. Thanks to Anne-Sabine Grosjean who help for the selection and thin section preparation. Federica Schiavi assisted with the Raman analyses. Martin Robyr assisted with EPMA mappings. Marilynne Imbault, Mhamed Benbakkar and Krzysztof Suchorski assisted with the ICP-AES and ICPMS analyses. We thank Bertus Smith for fruitful discussion. Frances Westall and two anonymous reviewers gave us fruitful comments to improve the manuscript. This research was supported by the INSU Programme National de Planétologie and the European Union's Horizon H2020 research and innovation program ERC (STROMATA, grant agreement 759289), and by the French Government Laboratory of Excellence initiative n° ANR-10-LABX-0006, the Region Auvergne and the European Regional Development Fund. This is Laboratory of Excellence ClerVolc contribution number 486.

## Appendix A. Supplementary data

Supplementary data to this article can be found online at <https://doi.org/10.1016/j.precamres.2021.106306>.

## References

- Agangi, A., Hofmann, A., Elburg, M.A., 2018. A review of Palaeoproterozoic felsic volcanism in the eastern Kaapvaal craton: Linking plutonic and volcanic records. *Geosci. Frontiers* 9, 667–688.
- Agangi, A., Hofmann, A., Eickmann, B., Marin-Carbonne, J., 2019. Mesoarchaean Gold Mineralisation in the Barberton Greenstone Belt: A Review. In *The Archaean Geology of the Kaapvaal Craton, Southern Africa*; Kröner, A., Hofmann, A., Eds.; Springer Nature Switzerland AG: Cham, Switzerland, pp. 171–184.
- Alleon, J., Bernard, S., Le Guillou, C., Daval, D., Skouri-Panet, F., Pont, S., Delbes, L., Robert, F., 2016. Early entombment within silica minimizes the molecular degradation of microorganisms during advanced diagenesis. *Chem. Geol.* 437, 98–108.

- Alleon, J., Bernard, S., Le Guillou, C., Beyssac, O., Sugitani, K., Robert, F., 2018. Chemical nature of the 3.4 Ga Strelley Pool microfossils. *Geochem. Perspect. Lett.* 7, 37–42.
- Alleon, J., Bernard, S., Olivier, N., Thomazo, C.h., Marin-Carbonne, J., 2021. Inherited geochemical diversity of 3.4 Ga organic films from the Buck Reef Chert, South Africa. *Commun. Earth Environ.* 2, 6.
- Anhaeusser, C.R., 1976. The geology of the Sheba Hills area of the Barberton Mountain Land, South Africa: With particular reference to the Eureka Syncline. *Trans. Geol. Soc. South Afr.* 79, 253–280.
- Anhaeusser, C.R., Robb, L.J., Viljoen, M.J. 1981. Provisional geological map of the Barberton greenstone belt and surrounding granitic terrane, eastern Transvaal and Swaziland (1:250000). *Geol. Soc. South Afr. Spec. Pub.*
- Baccellini, L., Bosellini, A., 1965. Diagrammi per la stima visiva della composizione percentuale nelle rocce sedimentarie, *Annali Univ. Ferrara, N. S. Sez. IX, v. I*, pp. 59–62.
- Bonnand, P., Lalonde, S.V., Boyet, M., Heubeck, C., Homann, M., Nonnotte, P., Foster, I., Konhäuser, K.O., Köhler, I., 2020. Post-depositional REE mobility in a Paleoproterozoic banded iron formation revealed by La-Ce geochronology: A cautionary tale for signals of ancient oxygenation. *Earth Planet. Sci. Lett.* 547, 116452.
- Bower, D.M., 2011. Micro-Raman spectroscopic investigations of mineral assemblages in parallel to bedding laminae in 2.9 Ga sandstones of the Pongola Supergroup, South Africa. *J. Raman Spec.* 42, 1626–1633.
- Brookins, D.G. 1988. *Eh-pH Diagrams for Geochemistry*. Springer-Verlag.
- Condie, K.C., Viljoen, M.J., Kahle, E.J.D., 1977. Effects of alteration on element distributions in Archean tholeiites from the Barberton Greenstone Belt, South Africa. *Contrib. Mineral. Petrol.* 64, 75–89.
- Cuadrado, D.G., Bournaud, C.N., Pan, J., Carmona, N.B., 2013. Microbially-induced sedimentary structures (MISS) as record of storm action in supratidal modern estuarine setting. *Sed. Geol.* 296, 1–8.
- Cutts, K.A., Stevens, G., Hoffmann, J.E., Buick, I.S., Frei, D., Münker, C., 2014. Paleo- to Mesoarchean polymetamorphism in the Barberton Granite-Greenstone Belt, South Africa: Constraints from U-Pb monazite and Lu-Hf garnet geochronology on the tectonic processes that shaped the belt. *GSA Bull.* 126, 251–270.
- Davies, N.S., Liu, A.G., Gibling, M.R., Miller, R.F., 2016. Resolving MISS conceptions and misconceptions: A geological approach to sedimentary surface textures generated by microbial and abiotic processes. *Earth Sci. Rev.* 154, 210–246.
- Davies, N.S., Liu, A.G., Gibling, M.R., Miller, R.F., 2018. Reply to comment on the paper by Davies et al. "Resolving MISS conceptions and misconceptions: A geological approach to sedimentary surface textures generated by microbial and abiotic processes" (*Earth Science Reviews*, 154 (2016), 210–246). *Earth-Sci. Rev.* 176, 384–386.
- de Ronde, C.E.J., Kamo, S., Davis, D.W., de Wit, M.J., Spooner, E.T.C., 1991a. Field, geochemical and U-Pb isotopic constraints from hypabyssal felsic intrusions within the Barberton greenstone belt, South Africa: Implications for tectonics and the timing of gold mineralization. *Precam. Res.* 49, 261–280.
- de Ronde, C.E.J., Hall, C.M., York, D., Spooner, E.T.C., 1991b. Laser step-heating  $^{40}\text{Ar}/^{39}\text{Ar}$  age spectra from early Archean (~3.5 Ga) Barberton greenstone belt sediments: A technique for detecting cryptic tectono-thermal events. *Geochim. Cosmochim. Acta* 55, 1933–1951.
- de Ronde, C.E.J., Spooner, E.T.C., de Wit, M.J., Bray, C.J., 1992. Shear zone-related, Au quartz vein deposits in the Barberton Greenstone Belt, South Africa: Field and petrographic characteristics, fluid properties, and light stable isotope geochemistry. *Econ. Geol.* 87, 366–402.
- de Ronde, C.E.J., de Wit, M.J., 1994. Tectonic history of the Barberton greenstone belt, South Africa: 490 million years of Archean crustal evolution. *Tectonics* 13, 983–1005.
- de Wit, M.J., Hart, R.J., Martin, A., Abbott, P., 1982. Archean abiogenic and probable biogenic structures associated with mineralized hydrothermal vent systems and regional metamorphism, with implications for greenstone belt studies. *Econ. Geol.* 77, 1783–1802.
- Dunoyer de Segonzac, G., 1970. The transformation of clay minerals during diagenesis and low-grade metamorphism: A review. *Sedimentology* 10, 137–143.
- Eriksson, K.A., 1977. Tidal deposits from the Archean Moodies Group, Barberton Mountain Land, South Africa. *Sed. Geol.* 18, 257–281.
- Eriksson, K.A., 1978. Alluvial and destructive beach facies in the Archean Moodies Group of the Barberton Mountain Land. *Univ. Witwatersrand Johannesburg Economic Geol. Res. Unit Info. Circular* 115, 1–18.
- Eriksson, K.A., 1979. Marginal marine depositional processes from the Archean Moodies Group, Barberton Mountain Land, South Africa: Evidence and Significance. *Precam. Res.* 8, 153–182.
- Eriksson, K.A., 1980. Transitional sedimentation styles in the Moodies and Fig Tree Groups, Barberton Mountain Land, South Africa: Evidence favouring an Archean continental margin. *Precam. Res.* 12, 141–160.
- Eriksson, K.A., Simpson, E.L., 2000. Quantifying the oldest tidal record: The 3.2 Ga Moodies Group, Barberton Greenstone Belt, South Africa. *Geology* 28, 831–834.
- Eriksson, K.A., Simpson, E.L., Mueller, W., 2006. An unusual fluvial to tidal transition in the mesoarchean Moodies Group, South Africa: A response to high tidal range and active tectonics. *Sed. Geol.* 190, 13–24.
- Eriksson, K.A., Wilde, S.A., 2010. Palaeoenvironmental analysis of Archean siliciclastic sedimentary rocks in the west-central Jack Hills belt, Western Australia with new constraints on ages and correlations. *J. Geol. Soc.* 167, 827–840.
- Fabre, C., Devismes, D., Moncayo, S., Pelascini, F., Trichard, F., Lecomte, A., Bousquet, B., Cauzid, J., Motto-Ros, V., 2018. Elemental imaging by laser-induced breakdown spectroscopy for the geological characterization of minerals. *J. Anal. Atom. Spec.* 33, 1345–1353.
- Foucher, F., Westall, F., Knoll, A. 2012. Biosignatures observed by Raman mapping in silicified materials. *European Geosciences Union, General Assembly (Vol. 14, p. 4287)*. Vienna, Austria.
- Galvez, M.E., Beyssac, O., Benzerara, K., Menguy, N., Bernard, S., Cox, S.C., 2012. Micro- and nano-textural evidence of Ti-(Ca-Fe) mobility during fluid-rock interactions in carbonaceous lawsonite-bearing rocks from New Zealand. *Contrib. Mineral. Petrol.* 164, 895–914.
- Gamper, A., Heubeck, C., Demscek, D., 2011. Composition and microfacies of Archean microbial mats (Moodies Group, ca. 3.22 Ga, South Africa). In: Noffke, N., Chafetz, H. (Eds.), *Microbial Mats in Siliciclastic Depositional Systems Through Time*, SEPM Soc. Sed. Geol., pp. 65–74.
- Gerdes, G., Klenke, T., Noffke, N., 2000. Microbial signatures in peritidal siliciclastic sediments: A catalogue. *Sedimentology* 47, 279–308.
- Gerdes, G., Klenke, T., 2007. States of biogenic bedding as records of the interplay of ecologic time and environment (a case study of modern siliciclastic sediments, Mellum Island, southern North Sea). *Senckenb. Marit* 37, 129–144.
- Glamoclija, M., Steele, A., Fries, M., Schieber, J., Voytek, M.A., Cockell, C.S. 2009. Association of anatase (TiO<sub>2</sub>) and microbes: Unusual fossilization effect or a potential biosignature? In: Gohn, G.S., Koerber, C., Miller, K.G., Reimold, W.U. (Eds.), *The ICDP-USGS Deep Drilling Project in the Chesapeake Bay Impact Structure: Results from the Eyreville Core Holes*, GSA Spec. Pap. 458, pp. 965–975.
- Hessler, A.M., Lowe, D.R., 2006. Weathering and sediment generation in the Archean: An integrated study of the evolution of siliciclastic sedimentary rocks of the 3.2 Ga Moodies Group, Barberton Greenstone Belt, South Africa. *Precam. Res.* 151, 185–210.
- Heubeck, C., 2009. An early ecosystem of Archean tidal microbial mats (Moodies Group, South Africa, ca. 3.2 Ga). *Geology* 37, 931–934.
- Heubeck, C., 2019. The Moodies Group—A High-resolution archive of archaean surface processes and basin-forming mechanisms. In: Kröner, A., Hofmann, A. (Eds.), *The Archean Geology of the Kaapvaal Craton, Southern Africa*. Regional Geology Reviews, Springer Nature Switzerland AG, pp. 133–169.
- Heubeck, C., Lowe, D.R., 1994a. Depositional and tectonic setting of the Archean Moodies Group, Barberton Greenstone Belt, South Africa. *Precam. Res.* 68, 257–290.
- Heubeck, C., Lowe, D.R., 1994b. Late syndepositional deformation and detachment tectonics in the Barberton Greenstone-Belt, South-Africa. *Tectonics* 13, 1514–1536.
- Heubeck, C., Lowe, D.R., 1999. Sedimentary petrography and provenance of the Archean Moodies Group, Barberton Greenstone Belt. In: Lowe, D.R., Byerly, G.R. (Eds.), *Geologic Evolution of the Barberton Greenstone Belt*. South Africa, Geological Society of America, Boulder, pp. 259–286.
- Heubeck, C., Engelhardt, J., Byerly, G.R., Zeh, A., Sell, B., Luber, T., Lowe, D.R., 2013. Timing of deposition and deformation of the Moodies Group (Barberton Greenstone Belt, South Africa): Very-high-resolution of Archean surface processes. *Precam. Res.* 231, 236–262.
- Heubeck, C., Bläsing, S., Grund, M., Drabon, N., Homann, M., Nabhan, S., 2016. Geological constraints on Archean (3.22 Ga) coastal-zone processes from the Dycedale Syncline, Barberton Greenstone Belt. *South African J. Geol.* 119, 495–518.
- Hickman-Lewis, K., Cavalazzi, B., Foucher, F., Westall, F., 2018. Most ancient evidence for life in the Barberton greenstone belt: Microbial mats and biofabrics of the ~3.47 Ga Middle Marker horizon. *Precam. Res.* 312, 45–67.
- Hickman-Lewis, K., Westall, F., Cavalazzi, B., 2019. Traces of early life from the Barberton Greenstone Belt, South Africa. In: Van Kranendonk, M., Bennett, V., Hoffmann, E. (Eds.), *Earth's Oldest Rocks*, 2nd edition. Elsevier B.V., pp. 1029–1058.
- Hickman-Lewis, K., Westall, F., Cavalazzi, B., 2020. Diverse communities of bacteria and archaea flourished in Palaeoarchean (3.5–3.3 Ga) microbial mats. *Palaeontology* 63, 1007–1033.
- Hofmann, A., 2005. The geochemistry of sedimentary rocks from the Fig Tree Group, Barberton greenstone belt: Implications for tectonic, hydrothermal and surface processes during mid-Archean times. *Precam. Res.* 143, 23–49.
- Hofmann, A., Bolhar, R., 2007. Carbonaceous Cherts in the Barberton Greenstone Belt and their significance for the study of Early Life in the Archean Record. *Astrobiology* 7, 355–388.
- Hofmann, A., Bolhar, R., Orberger, B., Foucher, F., 2013. Cherts of the Barberton Greenstone Belt, South Africa: Petrology and trace-element geochemistry of 3.5 to 3.3 Ga old silicified volcanoclastic sediments. *South Afr. J. Geol.* 116, 297–322.
- Homann, M., 2019. Earliest life on earth: Evidence from the Barberton Greenstone Belt. *South Africa. Earth Sci. Rev.* 196, 102888.
- Homann, M., Heubeck, C., Airo, A., Tice, M.M., 2015. Morphological adaptations of 3.22 Ga-old tufted microbial mats to Archean coastal habitats (Moodies Group, Barberton Greenstone Belt, South Africa). *Precam. Res.* 266, 47–64.
- Homann, M., Sansjofre, P., Van Zuilen, M., Heubeck, C., Gong, J., Killingsworth, B., Foster, I.S., Airo, A., Van Kranendonk, M.J., Ader, M., Lalonde, S.V., 2018. Microbial life and biogeochemical cycling on land 3,220 million years ago. *Nat. Geosci.* 11, 665–671.
- Igisi, M., Yokoyama, T., Ueno, Y., Nakashima, S., Shimajima, M., Ohta, H., Maruyama, S., 2018. Changes of aliphatic C-H bonds in cyanobacteria during experimental thermal maturation in the presence or absence of silica as evaluated by FTIR microspectroscopy. *Geobiology* 16, 412–428.
- Kamber, B.S., Greig, A., Collerson, K.D., 2005. A new estimate for the composition of weathered young upper continental crust from alluvial sediments, Queensland. *Australia. Geochim. Cosmochim. Acta* 69, 1041–1058.
- Knauth, L.P., Lowe, D.R., 1978. Oxygen isotope geochemistry of cherts from the Onverwacht Group (3.4 billion years), Transvaal, South Africa, with implications for secular variations in the isotopic composition of cherts. *Earth Planet. Sci. Lett.* 41, 209–222.

- Köhler, I., Heubeck, C., 2019. Microbial-mat-associated tephra of the Archean Moodies Group, Barberton Greenstone Belt (BGB), South Africa: Resemblance to potential biostructures and ecological implications. *South Afr. J. Geol.* 122, 221–236.
- Kröner, A., Nagel, T.J., Hoffmann, J.E., Liu, X., Wong, J., Hegner, E., Xie, H., Kasper, U., Hofmann, A., Liu, D., 2018. High-temperature metamorphism and crustal melting at ca. 3.2 Ga in the eastern Kaapvaal craton, southern Africa. *Precam. Res.* 317, 101–116.
- Lécuyer, C., Gruau, G., Anhaeusser, C.R., Fourcade, S., 1994. The origin of fluids and the effects of metamorphism on the primary chemical compositions of Barberton komatiites: New evidence from geochemical (REE) and isotopic (Nd, O, H, <sup>39</sup>Ar/<sup>40</sup>Ar) data. *Geochim. Cosmochim. Acta* 58, 969–984.
- Lekele Baghekema, S.G., Lepot, K., Riboulleau, A., Fadel, A., Trentesaux, A., El Albani, A., 2017. Nanoscale analysis of preservation of ca. 2.1 Ga old Francevillian microfossils. *Gabon. Precam. Res.* 301, 1–18.
- Lepot, K., 2020. Signatures of early microbial life from the Archean (4 to 2.5 Ga) eon. *Earth Sci. Rev.* 103296.
- Lowe, D.R., 1975. Water escape structures in coarse-grained sediments. *Sedimentology* 22, 157–204.
- Lowe, D.R., 1999. Petrology and sedimentology of cherts and related silicified sedimentary rocks in the Swaziland Supergroup. *Geol. Soc. Am. Spec. Pap.* 329, 83–114.
- Lowe, D.R., Byerly, G.R., Heubeck, C., 1999. Structural divisions and development of the west-central part of the Barberton Greenstone Belt. *Geol. Soc. Am. Spec. Pap.* 329, 37–82.
- Marin-Carbonne, J., Remusat, L., Sforza, M.C., Thomazo, C., Cartigny, P., Philippot, P., 2018. Sulfur isotope's signal of nanopyrites enclosed in 2.7 Ga stromatolitic organic remains reveal microbial sulfate reduction. *Geobiology* 16, 1–18.
- Mariotti, G., Pruss, S.B., Perron, J.T., Bosak, T., 2014. Microbial shaping of sedimentary wrinkle structures. *Nat. Geosci.* 7, 736–740.
- McBride, E.F., 1989. Quartz Cement in Sandstones: A Review. *Earth Sci. Rev.* 26, 69–112.
- McDonough, W.F., Sun, S., 1995. The composition of the Earth. *Chem. Geol.* 120, 223–253.
- McLennan, S.M., 1989. Rare earth elements in sedimentary rocks: Influence of provenance and diagenetic processes. *Geochemistry and Mineralogy of Rare Earth Elements. Rev. Mineral.* 21, 169–200.
- McLennan, S.M., Taylor, S.R., 1983. Geochemical evolution of Archean shales from South Africa. I. The Swaziland and Pongola Supergroups. *Precam. Res.* 22, 93–124.
- Munyai, M.R., Dirks, P.H.G.M., Charlesworth, E.G., 2011. Archaeological mineralisation during post-orogenic extension in the New Consort gold mine, Barberton Greenstone Belt, South Africa. *South Afr. J. Geol.* 114, 121–144.
- Motto-Ros, V., Gardette, V., Sancey, L., Leprince, M., Genty, D., Roux, S., Busser, B., Pelascini, F., 2020. LIBS-Based Imaging: Recent Advances and Future Directions. *Spectroscopy* 35, 34–40.
- Moyen, J.-F., Stevens, G., Kisters, A.F.M., Belcher, R.W., Lemirre, B., 2019. TTG Plutons of the Barberton Granitoid-Greenstone Terrain, South Africa. In: Van Kranendonk, M., Bennett, V., Hoffmann, E. (Eds.), *Earth's Oldest Rocks*, 2nd edition. Elsevier B.V., pp. 615–653.
- Nabhan, S., Köhler, I., Heubeck, C., 2017. Local and regional controls on the maturation state of carbonaceous matter in the Barberton Greenstone Belt. In: *Annual Meeting DGGV Bremen 2017, Bremen, Germany, 24–29 September*, abstract volume, p. 449.
- Newman, S.A., Klepac-Ceraj, V., Mariotti, G., Pruss, S.B., Watson, N., Bosak, T., 2017. Experimental fossilization of mat-forming cyanobacteria in coarse-grained siliciclastic sediments. *Geobiology* 15, 484–498.
- Noffke, N., 2007. Microbially induced sedimentary structures in Archean sandstones: A new window into early life. *Gondwana Res.* 11, 336–342.
- Noffke, N., 2010. *Geobiology: Microbial mats in sandy deposits from the Archean era to today*. Springer 1–194.
- Noffke, N., 2018. Comment on the paper by Davies et al. “Resolving MISS conceptions and misconceptions: A geological approach to sedimentary surface textures generated by microbial and abiotic processes” (*Earth Science Reviews*, 154 (2016), 210–246). *Earth Sci. Rev.* 176, 373–383.
- Noffke, N., Gerdes, G., Klenke, T., Krumbein, W.E., 1997. A microscopic sedimentary succession of graded sand and microbial mats in modern siliciclastic tidal flats. *Sed. Geol.* 110, 1–6.
- Noffke, N., Gerdes, G., Klenke, T., Krumbein, W.E., 2001. Microbially induced sedimentary structures – A new category within the classification of primary sedimentary structures. *J. Sed. Res.* 71, 649–656.
- Noffke, N., Hazen, R.M., Nhlleko, N., 2003. Earth's earliest microbial mats in a siliciclastic marine environment (2.9 Ga Mozaan Group, South Africa). *Geology* 31, 673–676.
- Noffke, N., Eriksson, K.A., Hazen, R.M., Simpson, Edward L., 2006. A new window into Early Archean life: Microbial mats in Earth's oldest siliciclastic tidal deposits (3.2 Ga Moodies Group, South Africa). *Geology* 34 (4), 253–256.
- Noffke, N., Beukes, N., Bower, D., Hazen, R.M., Swift, D.J.P., 2008. An actualistic perspective into Archean worlds – (cyano-)bacterially induced sedimentary structures in the siliciclastic Nhlazatse Section, 2.9 Ga Pongola Supergroup, South Africa. *Geobiology* 6, 5–20.
- Noffke, N., Christian, D., Wacey, D., Hazen, R.M., 2013. Microbially Induced Sedimentary Structures Recording an Ancient Ecosystem in the ca. 3.48 Billion-Year-Old Dresser Formation, Pilbara, Western Australia. *Astrobiology* 13, 1103–1124.
- Pasteris, J.D., Brigitte Wopenka, B., 2003. Necessary, but not sufficient: Raman identification of disordered carbon as a signature of ancient life. *Astrobiology* 3 (4), 727–738.
- Pe-Piper, G., Karim, A., Piper, D.J.W., 2011. Authigenesis of titania minerals and the mobility of Ti: New evidence from pro-deltaic sandstones, cretaceous Scotian Basin, Canada. *J. Sed. Res.* 81, 762–773.
- Petsch, S.T., Berner, R.A., Eglinton, T.I., 2000. A field study of the chemical weathering of ancient sedimentary organic matter. *Org. Geochem.* 31, 475–487.
- Richards, J.P., Krogh, T.E., Spooner, E.T.C., 1988. Fluid Inclusion characteristics and U-Pb rutile age of late hydrothermal alteration and veining at the Musoshi Stratiform Copper Deposit, Central African Copper Belt, Zaire. *Econ. Geol.* 83, 118–139.
- Rudnick, R.L., Gao, S., 2014. 4.1 - Composition of the Continental Crust. In: *Treatise on Geochemistry* (ed. H. D. H. K. Turekian), second ed. Elsevier, Oxford, pp. 1–51.
- Saitoh, M., Nabhan, S., Thomazo, C., Olivier, N., Moyen, J.-F., Ueno, Y., Marin-Carbonne, J., 2020. Multiple Sulfur Isotope Records of the 3.22 Ga Moodies Group, Barberton Greenstone Belt. *Geosciences* 10, 145, <https://dx.doi.org/10.3390/geosciences10040145>.
- Sancey, L., Motto-Ros, V., Busser, B., Kotb, S., Benoit, J.M., Piednoir, A., Lux, F., Tillement, O., Panczer, G., Yu, J., 2014. Laser spectrometry for multi-elemental imaging of biological tissues. *Sci. Rep.* 4, 6065.
- Sanchez-Garrido, C.J.M.G., Stevens, G., Armstrong, R.A., Moyen, J.-F., Martin, H., Doucelean, R., 2011. Diversity in Earth's early felsic crust: Paleoproterozoic peraluminous granites of the Barberton Greenstone Belt. *Geology* 39, 963–966.
- Selvaraja, V., Caruso, S., Fiorentini, M.L., LaFlamme, C.K., Bui, T.H., 2017. Atmospheric sulfur in the orogenic gold deposits of the Archean Yilgarn Craton, Australia. *Geology* 45, 691–694.
- Simpson, E.L., Eriksson, K.A., Mueller, W.U., 2012. 3.2 Ga eolian deposits from the Moodies Group, Barberton Greenstone Belt, South Africa: Implications for the origin of first-cycle quartz sandstones. *Precam. Res.* 214–215, 185–191.
- Singh, P., 2009. Major, trace and REE geochemistry of the Ganga River sediments: Influence of provenance and sedimentary processes. *Chem. Geol.* 266, 242–255.
- Sirantoine, E., Wacey, D., Bischoff, K., Saunders, M., 2020. Authigenic anatase within 1 billion-year-old cells. *Geobiology* 2020 (00), e12417.
- Smith, S.J., Stevens, R., Liu, S.F., Li, G.S., Navrotsky, A., Boerio-Goates, J., Woodfield, B. F., 2009. Heat capacities and thermodynamic functions of TiO<sub>2</sub> anatase and rutile: Analysis of phase stability. *Am. Mineral.* 94, 236–243.
- Tada, R., Siever, R., 1989. Pressure solution during diagenesis. *Ann. Rev. Earth Planet. Sci.* 17, 89–118.
- Taylor, J., Stevens, G., Buick, I.S., Lana, C., 2012. Successive midcrustal, high-grade metamorphic events provide insight into Mid-Archean mountain-building along the SE margin of the proto-Kaapvaal craton. *GSA Bull.* 124, 1191–1211.
- Thomazo, C., Couradeau, E., Giraldo-Silva, A., Marin-Carbonne, J., Brayard, A., Homann, M., Sansjofre, P., Lalonde, S.V., Garcia-Pichel, F., 2020. Carbon and nitrogen isotope biosignatures of the archean continental biosphere: A comparison with modern analogs. *Astrobiology*. <https://doi.org/10.1089/ast.2019.2144>.
- Toulkeridis, T., Goldstein, S.L., Clauer, N., Kröner, A., Lowe, D.R., 1994. Sm-Nd dating of Fig Tree clay minerals of the Barberton greenstone belt, South Africa. *Geology* 22, 199–202.
- Toulkeridis, T., Goldstein, S.L., Clauer, N., Kröner, A., Todt, W., Schidlowski, M., 1998. Sm-Nd, Rb-Sr and Pb-Pb dating of silicic carbonates from the early Archean Barberton Greenstone Belt, South Africa: Evidence for post-depositional isotopic resetting at low temperature. *Precam. Res.* 92, 129–144.
- Toulkeridis, T., Clauer, N., Kröner, A., Todt, W., 2015. A mineralogical, chemical and isotopic investigation of shales from the Barberton Greenstone Belt, South Africa, to constrain source materials and postdeposition evolution. *South Afr. J. Geol.* 118, 389–410.
- Van Kranendonk, M.J., 2006. Volcanic degassing, hydrothermal circulation and the flourishing of early life on Earth: A review of the evidence from c. 3490–3240 Ma rocks of the Pilbara Supergroup, Pilbara Craton, Western Australia. *Earth Sci. Rev.* 74, 197–240.
- Van Zuilen, M.A., Chaussidon, M., Rollion-Bard, C., Marty, B., 2007. Carbonaceous cherts of the Barberton Greenstone Belt, South Africa: Isotopic, chemical and structural characteristics of individual microstructures. *Geochim. Cosmochim. Acta* 71, 655–669.
- Wacey, D., 2009. *Early Life on Earth: A Practical Guide*, Springer, Heidelberg, pp. 1–267.
- Wang, H., Yang, J.H., Kröner, A., Zhu, Y.S., Wei, Q.D., Li, R., Xu, L., 2020. Extensive magmatism and metamorphism at ca. 3.2 Ga in the eastern Kaapvaal Craton. *Precam. Res.* 351, 105952.
- Weis, D., Wasserburg, G.J., 1987. Rb-Sr and Sm-Nd isotope geochemistry and chronology of cherts from the Onverwacht Group (3.5 AE), South Africa. *Geochim. Cosmochim. Acta* 51, 973–984.
- Westall, F., 2008. Morphological biosignatures in early terrestrial and extraterrestrial materials. *Space Sci. Rev.* 135, 95–114.
- Westall, F., Cavalazzi, B., Lemelle, L., Marrocchi, Y., Rouzaud, J.-N., Simionovici, A., Salomé, M., Mostefaoui, S., Andreazza, C., Foucher, F., Toporski, J., Jaus, A., Thiel, V., Southam, G., MacLean, L., Wirick, S., Hofmann, A., Meibom, A., Robert, F., Défarge, C., 2011. Implications of in situ calcification for photosynthesis in a ~3.3 Ga-old microbial biofilm from the Barberton greenstone belt, South Africa. *Earth Planet. Sci. Lett.* 310, 468–479.
- Westall, F., Hickman-Lewis, K., Cavalazzi, B., 2018. Biosignatures in deep time. In: Cavalazzi, B., Westall, F. (Eds.), *Biosignatures for Astrobiology. Advances in Astrobiology and Biogeophysics*, Springer Nature Switzerland AG, pp. 145–164.
- Zhang, W., Hu, Z.C., Liu, Y.S., Chen, H.H., Gao, S., Gaschnig, R.M., 2012. Total rock dissolution using ammonium bifluoride (NH<sub>4</sub>HF<sub>2</sub>) in screw-top teflon vials: A new development in open-vessel digestion. *Anal. Chem.* 84, 10686–10693.